communications biology

A Nature Portfolio journal

Article

https://doi.org/10.1038/s42003-025-09385-x

Canine parvovirus infection affects host cell nucleolar organization and ribosome biogenesis

Moona Huttunen[1,7], **Satu Hakanen**[1,7], **Vesa Aho**[1], **Simon Leclerc**[1], **Aynur Soenmez**[2], **Sergey Kapishnikov**[3], **Alessandro Zannotti**[3], **Visa Ruokolainen**[1], **Kari Salokas**[4], **Markku Varjosalo**[4], **Leena Latonen**[5], **Colin R. Parrish**[6], **Kenneth Fahy**[3], **Salla Mattola**[1], **Denis L. J. Lafontaine**[2,7] ✉ & **Maija Vihinen-Ranta**[1,7] ✉

The nucleolus is a biomolecular condensate essential for ribosome biogenesis and cellular stress response, and it is a key target for many DNA viruses. However, little is known about how autonomous parvovirus infection impacts the nucleolus. Here, we used ten-fold robust expansion microscopy, cryo soft X-ray tomography, interactomics, and biochemical approaches to study nucleolar remodeling during canine parvovirus infection. The nucleolus is organised in nested layers. Infection led to redistribution of nucleolar upstream binding transcription factor 1 (inner core), fibrillarin (middle layer), and Ki-67 (outer rim). In contrast, peripheral nucleolar proteins (nucleolin and nucleophosmin) and precursor ribosomal RNAs remain in spherical structures. High-resolution microscopy revealed profound nucleolar structural changes, including thickened perinucleolar chromatin and enlarged nucleolar low-protein density channels. BioID identified interactions between viral NS2 and nucleolar proteins involved in ribosome biogenesis. Northern blotting demonstrated a slowdown in ribosome biogenesis during infection. Collectively, these findings provide insights into how parvoviruses remodel nucleolar structure and function.

Interaction with a multifunctional subnuclear compartment, the nucleolus, is crucial for the replication and pathogenesis of several DNA viruses, including herpesviruses[1,2] and adenoviruses[3–5]. Moreover, the capsids of adeno-associated virus (AAV), a helper-dependent parvovirus, are assembled in the nucleolus[6,7]. The role of nucleoli in the autonomous parvovirus life cycle has remained unexplored.

The nucleolus is the largest nuclear subcompartment, and it is involved in the initial steps of ribosome biogenesis, such as transcription of ribosomal RNA genes (rRNA), processing and modification of precursor rRNAs (pre-rRNAs), and ribosome subunit assembly[8,9]. The events of ribosome production are most likely coordinated, at least in part, by liquid–liquid phase separation[10,11]. The nucleolus is surrounded by heterochromatin and euchromatin, forming a stable nucleolus-nucleoplasm interface around the nucleoli[12–15]. The mammalian nucleolus comprises three main morphological components: the fibrillar center (FC), the dense fibrillar component (DFC), and the granular component (GC)[9,16–20]. Additional subphases have recently been identified by high-resolution fluorescence microscopy, including the periphery of the dense fibrillar center (PDFC) and the nucleolar rim (NR)[18,21]. FCs and DFCs are involved in rDNA transcription and initial maturation of pre-rRNAs, whereas further processing of pre-rRNAs and assembly of ribosome subunits occur in GC[9,16,17]. The nucleolus is a dynamic structure[22–25] with highly mobile proteins constantly shuttling between the nucleolus and the nucleoplasm[26,27]. The nucleolus has many additional functions besides ribosomal biogenesis, including the regulation of mitosis and the cell cycle, and acting as a biosensor of stresses of different origins, such as oxidative stress, heat shock, nutrient deprivation, and viral infection[28–32].

---

[1] Department of Biological and Environmental Science and Nanoscience Center, University of Jyvaskyla, Jyvaskyla, Finland. [2] RNA Molecular Biology, Fonds de la Recherche Scientifique (F.R.S./FNRS), Biopark campus, Université libre de Bruxelles (ULB), B-Gosselies, Bruxelles, Belgium. [3] SiriusXT Limited, Dublin, Ireland. [4] Institute of Biotechnology and Helsinki Institute of Life Science (HiLIFE), University of Helsinki, Helsinki, Finland. [5] Institute of Biomedicine, University of Eastern Finland, Kuopio, Finland. [6] Baker Institute for Animal Health, Department of Microbiology and Immunology, College of Veterinary Medicine, Cornell University, Ithaca, NY, USA. [7] These authors contributed equally: Moona Huttunen, Satu Hakanen, Denis L. J. Lafontaine, Maija Vihinen-Ranta.
✉ e-mail: denis.lafontaine@ulb.be; maija.vihinen-ranta@jyu.fi

The proper localization of several nucleolar proteins is profoundly affected by viral infection. In healthy cells, upstream-binding factor 1 (UBF1), fibrillarin (FBL), nucleolin (NCL), nucleophosmin 1 (NPM1), and proliferation marker protein Ki-67 are enriched in the nucleolar compartments FC, DFC, PDFC, GC, and NR, respectively[21,24]. In infected cells, some of these proteins are displaced and even relocated outside of the organelle[33–35]. One remarkable example is the abundant multifunctional phosphoprotein NCL[36–38], which relocalizes from the nucleolus to the viral replication compartments (VRC) upon infection with herpes simplex virus type 1 (HSV-1)[33–35] and other stresses[39,40]. NCL is a multifunctional factor implicated in virtually all stages of ribosome biogenesis[37,38], requiring its dynamic shuttling between the nucleolus and the nucleoplasm[41]. Other nucleolar proteins whose distribution is sensitive to stress include FBL, UBF1, and NPM1[42–44]. UBF1 is a transcription factor that binds specifically to the rDNA promoters and maintains the active state of rDNA[45–48]. FBL is a snoRNA-guided methyltransferase responsible for rRNA 2′-O methylation and a pre-rRNA-processing factor essential for the initial steps of ribosomal biogenesis[49–51]. In addition, FBL binds to nascent transcripts, helping their transition from the FC/DFC interphase to the DFC, where they undergo initial maturation[10]. NPM1 assists in ribosome assembly, chromatin modeling, and cell homeostasis[52]. NPM1 is a pentameric protein that mediates the assembly of the GC via heterotypic interactions with nucleolar proteins and rRNA and homotypic interactions with intrinsically disordered regions of nucleolar proteins[53,54]. Ki-67 is a “chromosome surfactant” protein located in the nucleoli in interphase cells and the mitotic chromosome periphery in mitotic cells[55,56]. During the interphase, Ki-67 has a specific role in the organization of heterochromatin[21,57,58]; during mitosis, it is essential to reassemble the nucleolus[21,24].

Autonomous parvoviruses have non-enveloped icosahedral particles of ~25 nm in diameter, enclosing a linear single-stranded DNA genome of ~5.0 kb. A typical parvovirus genome contains two open reading frames that encode several structural and non-structural proteins[59]. The canine parvovirus (CPV) capsid is composed of the structural viral proteins VP1 and VP2, with the latter also being N-terminally cleaved into a third structural protein, VP3, in mature virions[60]. CPV and other protoparvoviruses encode two non-structural proteins, NS1 and NS2[59]. The CPV NS1 protein is a multifunctional protein that exhibits site-specific DNA binding, ATPase, helicase, and nickase activities[61,62]. NS1 localizes into the nuclear VRC distributed throughout the nucleus but is absent from the nucleolar region[63]. NS2 of another protoparvovirus, the minute virus of mice, has been linked to viral DNA replication, translation of viral mRNA, capsid assembly, and pre-lytic nuclear egress[64–66]. Although the function of CPV NS2 is currently mostly undefined, our recent studies have revealed a potential role in chromatin remodeling and DNA damage response during replication[67].

Here, we investigated how CPV infection impacts nucleolar morphology and function. We show that infection leads to the redistribution of key nucleolar proteins and rRNA, extensive remodeling of nucleolar structure, and reorganization of nucleolus-associated chromatin. Notably, these alterations are accompanied by marked changes in pre-rRNA processing, highlighting the profound effects of CPV on nucleolar homeostasis.

Results

Nucleolar structure is remodeled during infection

To test if viral infection impacts nucleolus homeostasis and ribosome biogenesis, we analyzed the distribution of critical nucleolar proteins and rRNA in CPV-permissive Norden Laboratory Feline Kidney (NLFK) cells. We examined the distribution of representative markers of the major nucleolar compartments. We used UBF1, FBL, NCL, NPM1, and Ki-67 antibodies to label FC, DFC, PDFC, GC, and NR, respectively (Fig. 1a). NS1 detection was used as a proxy to follow the progression of CPV infection.

At 24 h post-infection (hpi), UBF1 and FBL were relocalized outside of the nucleolar region, forming small, punctate foci scattered throughout the nucleoplasmic space while retaining some residual localization in the nucleolus. The emergence of small viral NS1-positive foci, visible at 8 hpi, initiated the formation of the VRC (Supplementary Fig. 1). The expansion and coalescence of these foci eventually resulted in an enlarged VRC filling the entire nucleoplasm (Fig. 1b, c, Supplementary Figs. 1–5). Mean volume analysis confirmed that the average size of UBF1 and FBL foci within the nuclear area decreased as the infection progressed up to 24 hpi (Fig. 1d). This was accompanied by a reduction in the fraction of nuclear UBF1 and FBL signal detected in these foci (Fig. 1e), favoring a more diffuse staining pattern. Remarkably, the behavior of PDFC and GC proteins was distinctly different. NCL and NPM1 retained their association with nucleoli during the progression of infection. The circularity (roundness) of the NCL and NPM1 regions increased strikingly at late infection, indicating a change in phase behavior (Fig. 1f, g; Supplementary Figs. 3a and 4a). For NPM1, this effect could be quantified using the circularity index (Supplementary Fig. 4b). However, this index could not be computed reliably for NCL due to background noise from the antibody signal. The measurement of NCL-stained regions suggested that the volume of the nucleoli remained unchanged in infection (Supplementary Fig. 3b). Finally, Ki-67, representing the NR regions, was relocalized from the nucleoli into foci scattered throughout the nucleoplasm in infected cells (Fig. 1h, i). The infection resulted in a partial redistribution of Ki-67 from the nucleoli to the nucleoplasm at 8 hpi. At 12 hpi, Ki-67 was seen in the nucleoli and nucleoplasm, accumulating close to the NE, which likely correlates with the reorganization of the host cell chromatin close to the nuclear envelope as the infection progresses (Supplementary Fig. 5, see also below Fig. 3a). Later, at 24 hpi, Ki-67 showed a homogenous nuclear distribution with a few distinct small foci (Supplementary Fig. 5).

Quantitative 3D image analysis demonstrated that the volume of rRNA-containing nucleolar regions decreased (Fig. 2a, b). At the same time, the nucleolar intensity of rRNA remained unchanged at late infection compared to control cells (Fig. 2c). Importantly, similar to the observations with NMP1 (Fig. 1f, g, Supplementary Figs. 3a, and 4a, b), rRNA-containing nucleolar regions became increasingly circular in late infection at 24 hpi (Fig. 2d).

In conclusion, upon viral infection, the nucleolus appears to disassemble, starting from its inner core (FC and DFC), which loses integrity, while the more peripheral layers (PDFC and GC) remain somewhat organized but exhibit increased circularity. The NR, which lines the exterior of the nucleolus, is also lost.

Reorganization of nucleolar ultrastructure upon infection

Host chromatin displacement and marginalization near the nuclear envelope (NE) is observed at the late stages of parvovirus infection as the VRC expands[63]. Little is known about how the infection and infection-induced redistribution of chromatin affect the organization of nucleolus-associated chromatin.

We used ten-fold robust expansion microscopy (TREx) to examine nucleolar chromatin organization and overall protein distribution. TREx enables super-resolution imaging, approaching 25–30 nm resolution, using a conventional confocal microscope by embedding immunostained cell samples in a swellable hydrogel[68]. Labeling total protein with a fluorescent NHS ester dye reveals the nanoscale organization and protein intensity within nucleoli, while DAPI staining highlights chromatin distribution (Fig. 3a)[69].

The NHS ester labeling revealed protein accumulation in spherical, nucleolus-like regions within the central nuclear areas of both noninfected and infected NLFK cells at 24 hpi. Immunostaining for FBL showed that, in noninfected cells, FBL localized to protein-dense areas—corresponding to DFCs—as expected for typical nucleolar architecture (Fig. 3a). Consistent with earlier observations (Fig. 1c, e), TREx microscopy at 24 hpi confirmed substantial redistribution of FBL into numerous nucleoplasmic foci upon infection (Fig. 3a), in agreement with disassembly of the FCs and DFCs, previously inferred from the nucleolar release of UBF1 and FBL (Fig. 2a).

Analysis of DNA and total protein distribution revealed that in both noninfected and infected cells, chromatin remained condensed near the nuclear envelope and partially around nucleoli (Fig. 3a, b). However,

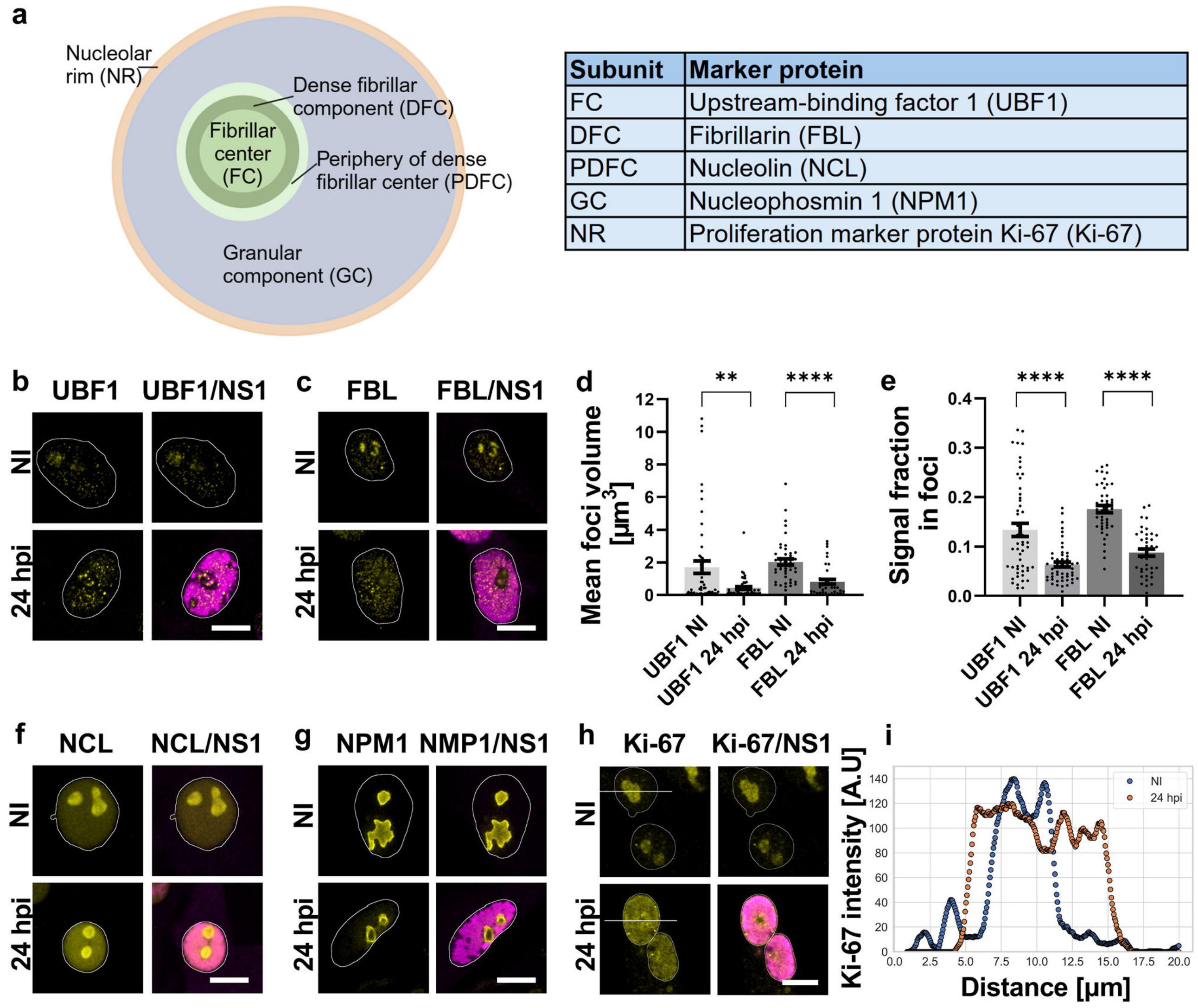

Subunit	Marker protein
FC	Upstream-binding factor 1 (UBF1)
DFC	Fibrillarin (FBL)
PDFC	Nucleolin (NCL)
GC	Nucleophosmin 1 (NPM1)
NR	Proliferation marker protein Ki-67 (Ki-67)

Fig. 1 | Nucleolar protein distribution changes during CPV infection. a Schematic of distribution of nucleolar proteins upstream-binding factor 1 (UBF1), fibrillarin (FBL), nucleolin (NCL), nucleophosmin 1 (NPM1), and Ki-67 in nucleolar subcompartments: the fibrillar center (FC), the dense fibrillar component (DFC), the periphery of the dense fibrillar center (PDFC), the granular component (GC), and the nucleolar rim (NR). Representative confocal maximum intensity projections showing the distribution of **b** UBF1 and **c** FBL in noninfected (NI) and infected NLFK cells at 24 hpi. **d** Quantitative analyses of the mean volume of UBF1 and FBL foci, and **e** the fraction of nuclear UBF1 and FBL signal detected in the foci in noninfected and infected cells at 24 hpi ($n_{\mathrm{NI}} = 52, 46$, and $n_{\mathrm{inf}} = 52, 40$, respectively). Distribution of **f** NCL, **g** NPM1, and **h** Ki-67 in noninfected and infected cells at 24 hpi. The white lines across the cells in (**h**) denote the pixels that were plotted in (**i**). **i** Representative Ki-67 intensity profiles in noninfected (blue) and infected cells (orange) at 24 hpi. The cells were immunolabeled with antibodies against UBF1, FBL, NCL, NPM1, and Ki-67 (yellow), as well as the viral NS1 protein (a marker of the viral replication compartment, magenta). DNA was labeled with DAPI, and a white line highlights the borders of the nuclei. Scale bar, 10 µm. The error bars show the standard error of the mean. Statistical significance was determined using Welch's *t*-test. The significance values shown are denoted as ****($p < 0.0001$) or **($p = 0.0021$). Figure 1a was created with BioRender.com.

perinucleolar chromatin intensity was markedly higher in infected cells, coinciding with reduced protein signal in these chromatin-dense zones (Fig. 3a, c).

In contrast, regions just inside the nucleolar border showed increased protein intensity during infection (Fig. 3c). The infection also led to a more irregular distribution of DNA within nucleoli, with the formation of large intra-nucleolar DNA foci and increased variability compared to noninfected cells (Fig. 3a, d). These foci coincided with areas of low protein density and were often surrounded by FBL, yet did not overlap with condensed perinucleolar DNA (Fig. 3a). This pattern suggests that the infection drives DNA accumulation in nucleolar interstices, as previously identified by EM studies[24,70,71]. Finally, infection also disrupted the spatial relationship between DNA and protein: whereas DNA and total protein signals were largely anti-correlated in noninfected cells, they became positively correlated upon infection (Fig. 3d, e).

The 3D reconstructions of TREx data demonstrated that the low-intensity protein regions formed interconnected channel networks, which sometimes spread throughout the nucleoli in noninfected and infected cells. In infected cells, the channels formed larger spherical vacuolar cavities, which were also interconnected. Notably, a substantial part of channels in noninfected and infected cells were DNA-containing interstices, or DNA was located close to the channels (Fig. 3f, Supplementary Movie 1).

To further examine the infection-induced changes in the 3D structure of nucleoli, NLFK cells were grown and infected on electron microscopy (EM) grids and analyzed using cryo soft X-ray tomography (cryo-SXT). Cryo-SXT allows label-free imaging of carbon- and nitrogen-containing cellular structures while preserving cells in a near-native frozen state and, as shown here, is particularly efficient in distinguishing normal and diseased-state nucleoli (Fig. 4). The attenuation of soft X-rays into intracellular structures creates biomolecule concentration- and composition-dependent

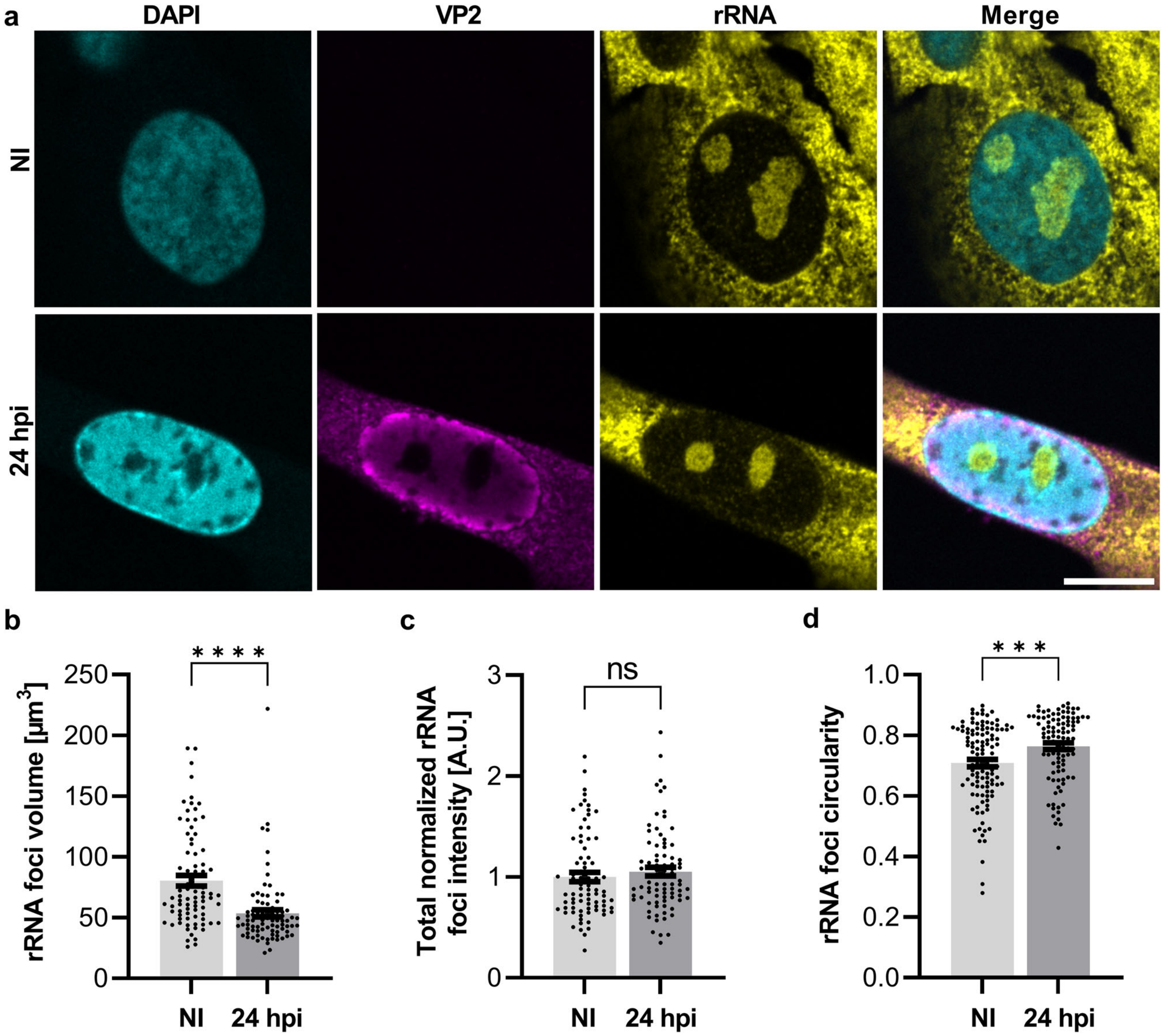

Fig. 2 | Infection decreases the size and increases the circularity of nucleolar rRNA-positive regions. a Representative confocal images displaying the distribution of viral capsids and rRNA in noninfected and infected NLFK cells at 24 hpi. The cells were stained with antibodies against the viral capsid protein VP2 (magenta) and rRNA (yellow). The chromatin was labeled with DAPI (cyan). Scale bar, 10 µm. **b** The mean volume, and **c** the total normalized intensity of segmented rRNA foci in noninfected and infected cells ($n = 82$ and 84, respectively). **d** The circularity of the rRNA-labeled segmented nucleoli cross-sections in noninfected and infected cells at 24 hpi ($n = 115$ and 100, respectively). The error bars show the standard error of the mean. Statistical significance was determined using Welch's *t*-test. The significance values shown are denoted as ****($p < 0.0001$), ***($p = 0.0009$), or ns (not significant).

images[72,73] from which quantitative features relevant to the material state of biomolecular condensates can be extracted. Notably, measurements of the linear absorption coefficient (LAC) provide a method to characterize nucleolar thickness and the distribution of low- and high-density regions of the nucleolus.

Cryo-SXT images and cross-sections of 3D cryo-SXT reconstruction data revealed misshapen nucleoli with an increased number of low-density foci at 24 hpi compared to noninfected cells (Fig. 4a, b, Supplementary Movie 2). The 3D analysis of the SXT data indicated that the roughness and the total LAC value of nucleoli (Fig. 4c, d) remained unchanged in infection. However, the nucleolar structure became heterogeneous with the increased appearance of infection-induced low-density foci (Fig. 4a, b). These foci are reminiscent of the low-protein density interstices observed using TREx (Fig. 3a). The number and total volume of these low-density foci increased during infection (Fig. 4e, f). Sometimes, individual foci formed thin, low-density connections extending from the NR towards the center of the nucleoli, as seen in noninfected cells (Fig. 4a, b). In our TREx studies, similar structures were observed to contain intranucleolar chromatin (Fig. 3a, f). Cryo-SXT analysis also revealed that the number of low-density regions was higher in infected than in noninfected cell nucleoli (Fig. 4g).

In conclusion, the high-resolution analysis of intranucleolar DNA and total protein content by expansion microscopy and cryo-SXT revealed the ultrastructural reorganization of nucleolar DNA and proteins, as well as the emergence of enlarged DNA-containing channels and low-density foci during CPV infection.

NS2 interacts with host cell proteins involved in nucleolar organization and rRNA processing

Our previous findings revealed that CPV NS2 localizes to the nucleolus during infection and that this protein may interact with nucleolar proteins[67]. To further investigate the extent of NS2 association with nucleolar proteins, we analyzed in greater detail our previously established NS2 interactome[67],

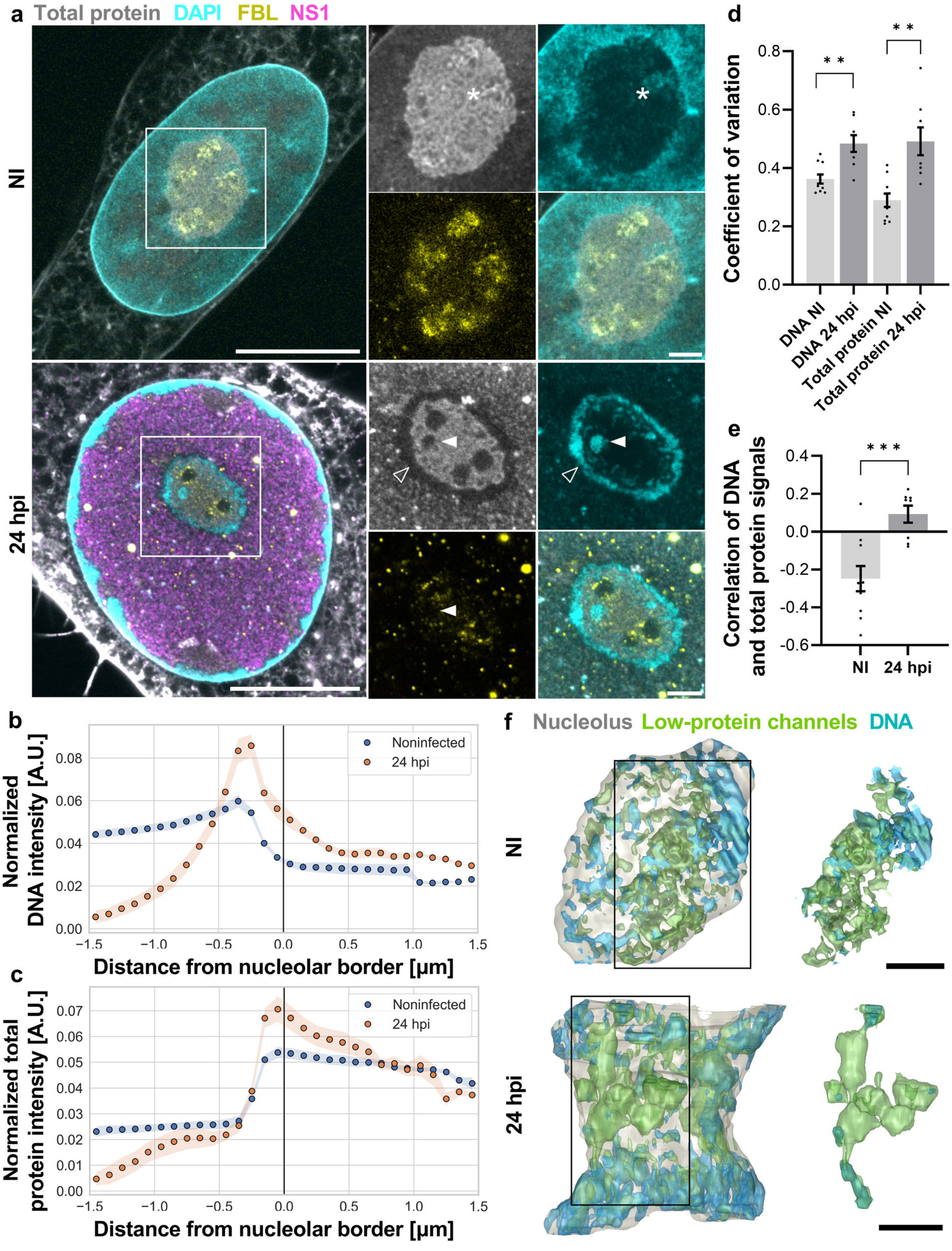

now focusing on the nucleolus. Our NS2 interactome was generated by proximity-dependent biotin identification (BioID) assays[74], and mass spectrometry analyses of NS2-associated proteins. Specifically, our dataset was produced using a BirA*-tagged NS2 fusion protein expressed in Flp-In T-Rex 293 cells infected with CPV (24 hpi) and, as a control, in noninfected cells.

The analysis of NS2-associated nucleolar proteins indicated that the number of proteins was slightly higher in noninfected cells (33 proteins) than in infected cells (27) (spectral count ≥ 2; Bayesian false discovery rate, BFDR, cutoff of <0.01 or <0.05) (Fig. 5a, b, Supplementary Data 1, 2). The NS2-associated proteins in noninfected cells represent putative interactions of NS2 independent of infection. In infected cells, most NS2-associated

Fig. 3 | Intranucleolar ultrastructure and chromatin distribution are remodeled in infection. a Visualization of the nucleolar structure by ten-fold robust expansion microscopy (TREx) in noninfected (NI) and infected NLFK cells at 24 hpi. The representative images show nuclear and nucleolar ultrastructures using the NHS ester total protein stain (gray), DNA staining by DAPI (cyan), and fibrillarin and viral NS1 using specific antibody staining (in yellow and magenta, respectively). The light areas in total protein-stained cells indicate the presence of highly concentrated protein, and dark areas indicate relatively small amounts of protein. The final expansion was estimated to be ~7.5-fold. The localization of nucleolar chromatin in noninfected cells (asterisks), perinucleolar chromatin (empty arrowheads), and nucleolar chromatin (filled arrowheads) in infected cells is shown. The intensities in each image have been independently adjusted for visualization purposes. Scale bars (adjusted to expansion factor), 5 and 1 μm. The mean normalized intensity of **b** DAPI-labeled DNA and **c** total protein as a function of the distance from the nucleolar border in noninfected and infected cells at 24 hpi ($n = 10$ and 8, respectively). **d** The distribution and dispersion of nucleolar DNA and total protein were measured using a coefficient of variation in noninfected and infected cells at 24 hpi. **e** DNA and total protein signal correlation in the nucleoli of noninfected and infected cells at 24 hpi **f** 3D reconstructions of TREx data show low-protein–concentration regions (green) and DNA-containing regions stained with DAPI (blue) within the nucleoli (gray) of noninfected and infected cells. Images on the right highlight a single, continuous low-protein–concentration channel network. Scale bar (adjusted to expansion factor), 1 µm. See also Supplementary Movie 1. Nucleolar segmentation was based on total protein staining. Error bars indicate the standard error of the mean. Statistical significance was determined using Welch's *t*-test, with significance levels denoted as ***($p = 0.0007$) and **($p = 0.0034$, $p = 0.0033$).

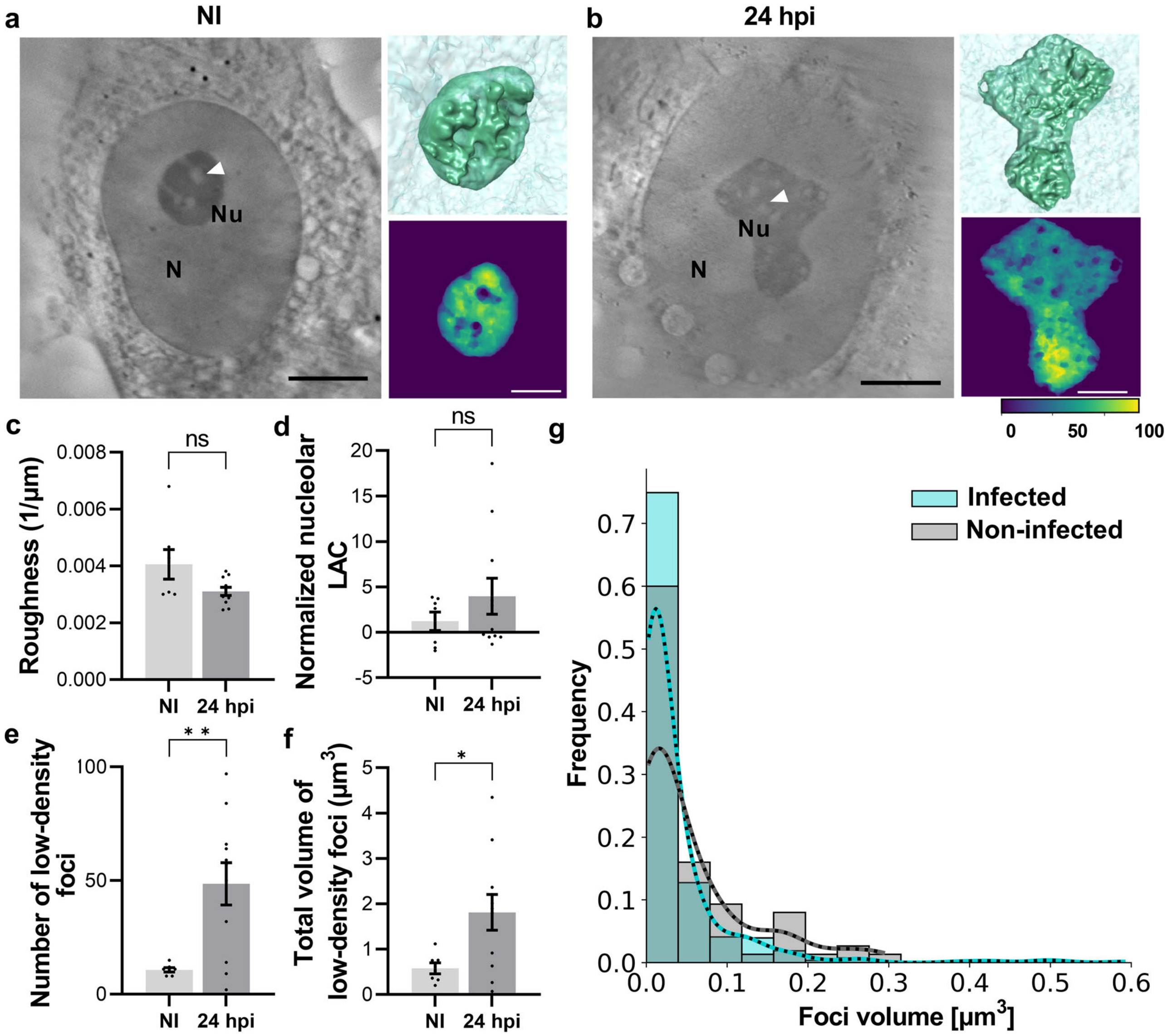

Fig. 4 | The progression of infection leads to appearance of small nucleolar foci with low density. Cryo-soft X-ray tomography (SXT) thin slices (orthoslices) of nucleus (N) and nucleoli (Nu) in **a** noninfected and **b** infected NLFK cells grown on EM grids at 24 hpi. 3D structure, enlarged insets of SXT reconstructions of nucleolar thickness, and the localization of nucleolar low-density foci and regions (filled arrowheads) are shown. The color scale indicates the thickness on the *Z*-axis (yellow, blue). Scale bars, 2.5 and 5 µm. See also Supplementary Movie 2. **c** Surface-to-volume ratio analysis of nucleolar roughness. **d** Nucleolar linear absorption coefficient LAC values, **e** the number, and **f** total volume of intranucleolar low-density foci. **g** The normalized number of various-sized nucleolar low-density foci in noninfected and infected cells ($n_{\mathrm{NI}} = 6$, $n_{\mathrm{inf}} = 7$). The error bars show the standard error of the mean. Statistical significance was determined using Welch's *t*-test. The significance values shown are denoted as **($p = 0.0023$), *($p = 0.0114$), or ns (not significant).

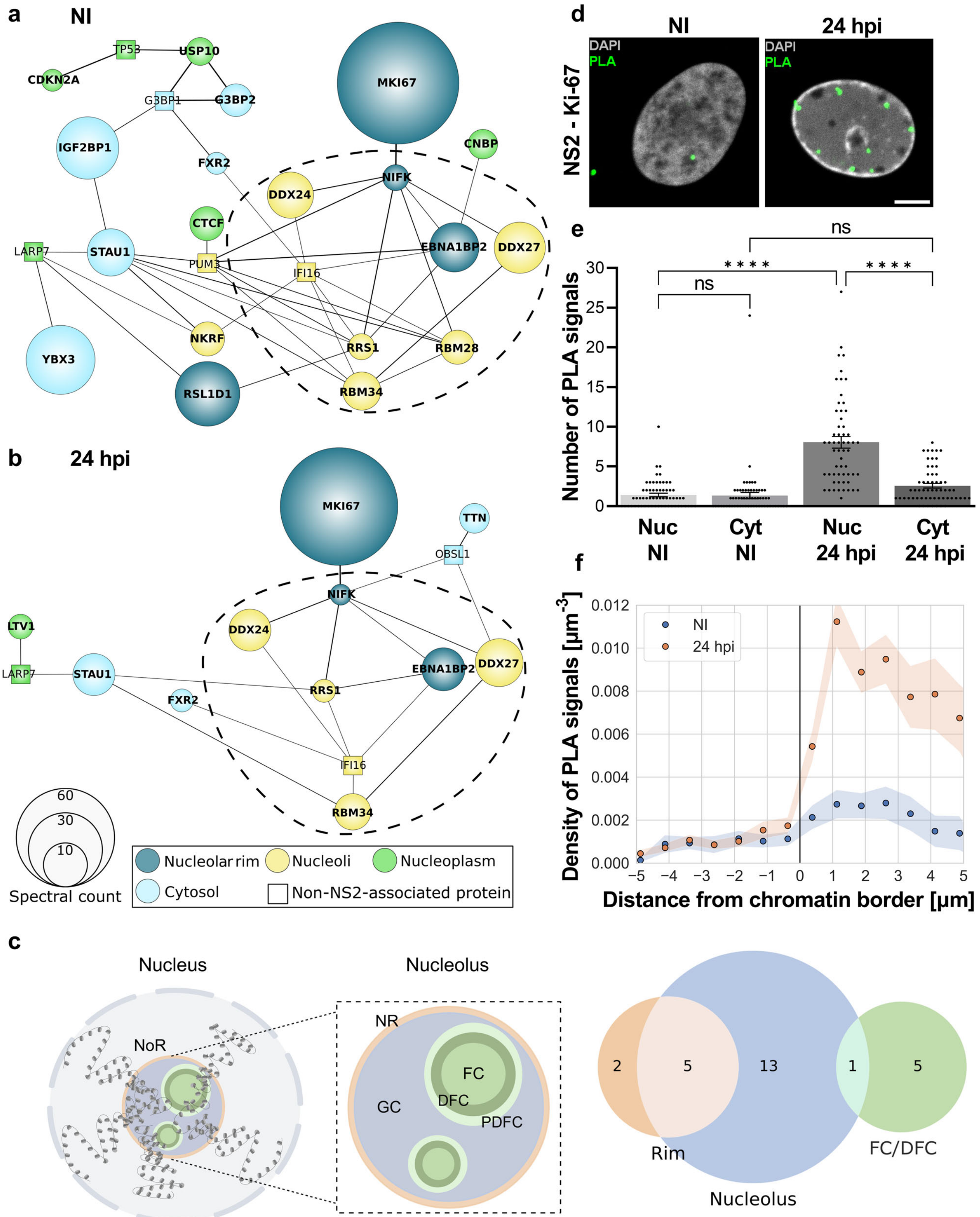

proteins with various biological functions were localized in the GC subcompartment of the nucleolus (20/27 of all spectral counts). Putative NS2 interactors were also located in the FC and DFC (six counts ≥ 2) and in the NR (seven counts ≥ 2), and some proteins showed dual localization (six) (Fig. 5c, Supplementary Data 1, 2). The highest-ranked high-confidence interactor detected by BioID was Ki-67 (MKI67), which was found in interaction with NS2 in both noninfected and infected cells (BFDR/spectral count 0.02/78.5 in infected and 0.04/76.5 in noninfected cells) (Fig. 5a, b, Supplementary Data 1, 2).

To confirm the association between Ki-67 and NS2, we used a Proximity Ligation Assay (PLA), which generates discrete fluorescent foci at sites of interactions detectable by light microscopy only when the two antigens

Fig. 5 | Nucleolar interactions of the viral NS2 protein. Schematic presentation of high-confidence BioID NS2 interactors related to nucleolar processes. Interactors of BirA*-tagged NS2 in **a** noninfected (NI) and **b** infected Flp-In T-REx 293 cells at 24 hpi are shown. All cells were transfected with BirA*-tagged NS2. Interactor proteins are presented by their gene names. The cellular distribution of NS2-associated nucleolar (round-shaped nodes) and non-nucleolar proteins (square-shaped nodes) in the nucleolar rim (dark blue), nucleoli (yellow), nucleoplasm (green), and cytosol (light blue) is shown. The node size correlates with interaction probability measured by spectral counts, and the black lines between nodes are proportional to the interaction in the STRING database (https://string-db.org/). Interactors are presented by their gene names. **c** A schematic image of the organization of the nucleolus organizer region (NoR), nucleolus, and its subcompartments: the fibrillar centre (FC), the dense fibrillar component (DFC), the periphery of dense fibrillar center (PDFC), the granular component (GC), and nucleolar rim (NR). The Venn diagram shows the nucleolar localization of NS2-associated proteins identified by BioID in infected cells at 24 hpi. The number of proteins localized into the whole nucleolus (blue), FC and DFC (green) nucleolar rim (orange), or dual localization (light brown, light green) is shown. **d** Representative confocal microscopy images showing the nuclear distribution of proximity ligation assay (PLA) foci, indicating the interaction between NS2 and Ki-67 in noninfected and infected cells at 24 hpi. Scale bar, 5 µm. **e** The number of PLA signals in the nucleus and cytoplasm. **f** The density of the PLA foci as a function of increasing distance from the NE in noninfected and infected cells ($n = 62$ and $n = 58$, respectively). The error bars and the shaded areas around the data points show the standard error of the mean. Statistical significance was determined using the Games–Howell test. The significance values shown are denoted as ****($p < 0.0001$) or * ($p = 0.0116$), or ns (not significant). Figure 5c was created with BioRender.com.

are within 40 nm of each other[75]. In noninfected cells, only very few foci per nucleus were detected (Fig. 5d). The number of foci in infected cells increased sharply, exhibiting a highly distinctive perinuclear distribution pattern, nearly perfectly concentric. Most punctate nuclear PLA signals were localized in the nucleoplasm near the NE (Fig. 5d, e), where chromatin accumulates (Fig. 3a). Most of the signals were accumulated in peripheral areas, not in the center of the nucleus (Fig. 5f). The negative NS2 and Ki-67 control in noninfected cells and technical probe controls (Fig. 5d, e, Supplementary Fig. 6) indicated that the background in the nuclear area was low.

Gene Ontology (GO) annotation analyses of biological processes indicated that 12 putative interaction partners of NS2 are involved in the organization of the nucleolus (GO:0007000, three proteins) and in pre-rRNA processing (GO:0006364, nine proteins) (Fig. 6a, Supplementary Data 1, 2). The nine proteins grouped for their involvement in pre-rRNA processing included three DEAD-box helicases: DDX27, DDX54, and DDX56. DDX27 (BFDR < 0.01) is essential for pre-rRNA synthesis, processing, and early ribosomal assembly, and it colocalizes with FBL in the DFC region[76,77].

We investigated whether the infection affects the subcellular distribution of three NS2-associated proteins: DDX27, the Epstein-Barr virus nuclear antigen 1 binding protein 2 (EBNA1BP2), and NIFK. In infected cells, DDX27 retained some nucleolar localization but was additionally accumulated in the nucleoplasm, showing increased nuclear intensity (Fig. 6b, c); the nucleoli also became rounder, as described above. The increased intensity of the DDX27 signal across the nucleus could be explained, at least in part, by increased protein levels (Supplementary Fig. 7a, b). EBNA1BP2 (BFDR < 0.05) is an NPM1-binding protein involved in ribosomal subunit assembly[78–80]. EBNA1BP2 was detected in the nucleolar area with decreased nuclear intensity in infected cells (Fig. 6d, e). NIFK, the nucleolar protein interacting with the FHA domain of Ki-67 (BFDR < 0.01), is an interactor of Ki-67 and NPM1 and participates in rRNA maturation, colocalizing with FBL in the DFC area[57,67,81,82]. Upon infection, NIFK was concentrated in the nucleolar area together with NS2 (Fig. 6f, g). For NIFK and EBNA1BP2, the change in signal intensity across the nucleus could not be explained by a change in protein levels (Supplementary Fig. 7a, c, d, e).

In conclusion, we detected several NS2-associated nucleolar proteins, including ribosome biogenesis factors, and demonstrated that the association of several of them with the nucleolus is affected upon infection.

Pre-rRNA processing is affected during CPV infection

To monitor how CPV infection may affect pre-rRNA processing, we analyzed rRNA intermediates using northern blotting in infected NLFK cells at 8, 12, and 24 hpi and, as a control, in noninfected cells (Fig. 7, Supplementary Fig. 8). The pre-rRNA processing pathway has not been described in felines, so we started by designing a set of probes specific to feline pre-rRNAs, targeting all four non-coding spacers (Fig. 7a). We used the rDNA of the *Felis catus* (domestic cat) genome as a reference (see Materials and methods). We modeled the feline pre-rRNA processing pathway on the well-characterized mouse one[83], a closely related vertebrate.

The most striking effects observed upon infection were: (1) a transient increase of several pre-rRNA species, observed at 8 and 12 hpi (these include the species 45S/47S, 36S, 32S, 18S-E, 12S, and species “e”), and (2) a decrease of others (notably of the 20S and “b”) (Fig. 7b, for quantification, see heat maps on Fig. 7c). These effects are consistent with inhibition of pre-rRNA processing at multiple cleavage sites, both early and late, resulting in a slowdown of ribosome production during viral infection (See Discussion).

These alterations of the steady-state levels of pre-rRNAs were perfectly reproducible, as shown by analysis in four independent biological replicates (Supplementary Fig. 8). Interestingly, a return to near normal pre-rRNA levels was observed at the latest time point of infection inspected, 24 hpi (e.g., compare levels of 47S/45S, 36S, or 12S in the NI and 24 hpi samples). Such recovery at a late stage of infection indicates that the inhibitions caused by the presence of the virus in cells are transient in nature. Nonetheless, at this late time point post-infection, the levels of 41S are strikingly higher than in noninfected cells, indicating some persistent effects of infection on pre-rRNA processing (Fig. 7c, d, Supplementary Data 3).

In conclusion, CPV infection of cells is accompanied by a transient yet substantial inhibition of pre-rRNA processing at specific cleavage sites across the pathway, leading to an unbalanced production of pre-rRNA precursors.

Discussion

A key feature of viruses is their ability to redirect cellular resources for their benefit, hijacking essential pathways and molecular nanomachines such as the ribosome and others. The nucleolus, the cell’s ribosome factory and central hub of energy consumption, is also a frequent target of viruses[84]. The nucleolus is rich in diverse catalytic activities, including folding, modification, and cleavage, that may benefit the virus. The nucleolus also functions as a biosensor that responds to diverse stresses, including viral infection, by remodeling its composition, morphology, and activity[30]. Many DNA viruses, such as HSV-1, adenovirus, and AAV, are known to target the nucleolus to interfere with host cell function and to direct their proteins there to facilitate viral replication[3,6,32,33,85]. However, the impact of autonomous parvovirus infection on nucleolar events has remained largely unknown. Our findings demonstrate that CPV infection induces profound structural and functional alterations of the nucleolus. These include disruption of the integrity of its internal layers, rounding up of its peripheral layers, and thickening of perinucleolar chromatin (Figs. 1–4). These structural changes are accompanied by inhibition of pre-rRNA processing (Fig. 7).

Viral infection has been reported to lead to striking changes in the nucleolar architecture and the redistribution of nucleolar proteins[32,86–88]. In HSV-1 infection, nucleolar UBF1 is relocalized from the FC to the VRC area, where it plays a role in viral replication[89]. In Kaposi’s sarcoma-associated herpesvirus, FBL is released into the nucleoplasm[88]. The methyltransferase activity of FBL is also essential for cytoplasmic replication of several pathogenic viruses, such as measles, mumps, and respiratory syncytial viruses[90]. In HSV-1 and cytomegalovirus infections, both NCL and NPM1

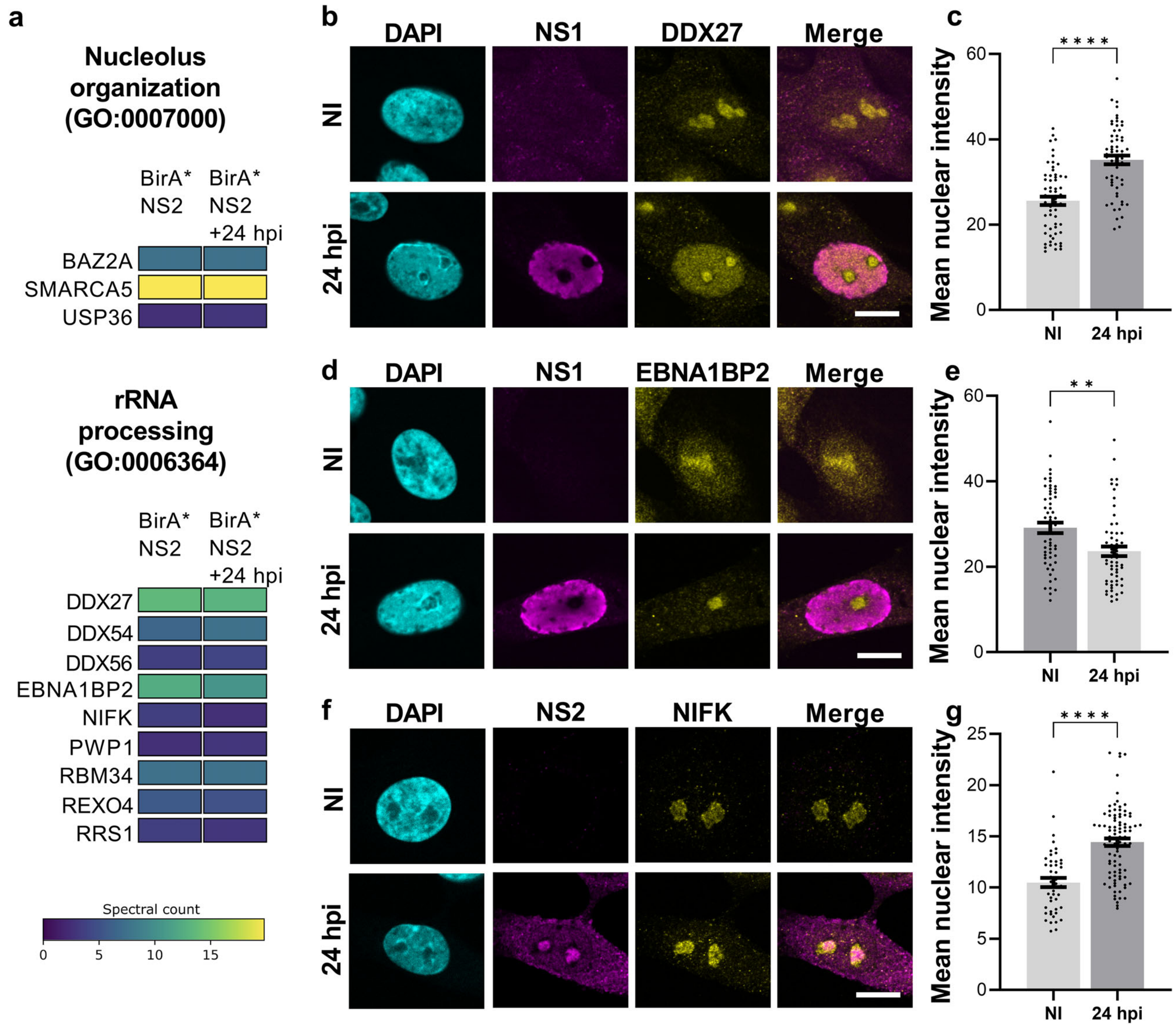

Fig. 6 | Distribution and intensity of NS2 interactor proteins are altered upon infection. a Identification of the viral NS2 protein nucleolar protein interactome using BioID. GO term classification for 12 high-confidence BioID NS2 interactors related to nucleolus organization and pre-rRNA processing. Interactors of BirA*-tagged NS2 in noninfected and infected Flp-In T-REx 293 cells at 24 hpi are shown. The color indicates spectral counts of each interactor in NS2-BioID experiments conducted with or without infection. Spectral counts are a measure of how many times a peptide of a given protein was matched in the MS/MS spectra. Similar spectral counts in both groups indicate that the association with NS2 occurs independently of other viral components. Interactors are presented by their gene names. **b** Representative confocal images of nuclear localization of DEAD-box helicase DDX27 and **c** mean nuclear intensity of DDX27 in noninfected and infected NLFK cells at 24 hpi ($n = 62$). **d** Nuclear distribution and **e** the mean nuclear intensity of EBNA1BP2 in noninfected and infected cells ($n = 59$). **f** Nuclear localization and **g** the mean nuclear intensity of NIFK in noninfected and infected cells ($n = 47$ and 92, respectively). The cells were immunolabeled with DDX27 (yellow), EBNA1BP2 (yellow), NIFK (yellow), and viral NS1 and NS2 protein (magenta) antibodies. DNA was labeled with DAPI (cyan). Scale bars, 10 µm. The error bars show the standard error of the mean. Statistical significance was determined using Welch's *t*-test. The significance values shown are denoted as ****($p < 0.0001$) and **($p = 0.0013 < 0.01$).

become dispersed into the nucleoplasm[33–35,91,92]. NPM1 is removed from the nucleoli by the endonuclease function of the HSV-1 endonuclease UL24[33,93]. Both cellular NCL and viral UL24 are essential for the nuclear egress of HSV-1 capsids[33,93,94]. This suggests a link between the HSV-1 infection-induced disruption of nucleolar structure integrity and viral egress.

This study focused on CPV infection and its impact on nucleolar architecture. Our findings indicate that the FC/DFC and NR substructures are disassembled during infection, resulting in the partial release of nucleolar marker proteins into the nucleoplasm. Remarkably, during the normal disassembly of the nucleolus at the onset of mitosis in cycling cells, the FC and DFC are also the first subphases to disappear[24], highlighting a parallel between nucleolar breakdown during mitosis and that induced by CPV infection. These results are consistent with our previous work, showing that CPV infection causes cell cycle arrest at the G2/M checkpoint, interfering with its release and the progression into early mitotic events[95].

At late stages of CPV infection, the nucleolar proteins UBF1 and FBL relocalized to the nucleoplasm, which was predominantly occupied by an enlarged VRC (Fig. 1). Remarkably, the PDFC and GC markers (NCL and NPM1, respectively) remained associated with the nucleolar area, forming protein-rich centers with increased circularity in late infection. Interestingly, NCL has earlier been shown to form complexes with the viral single-stranded genomes of MVM in vitro[96] and to bind AAV-2 capsids assembled in the nucleoli in vivo[6,7,97]. Our findings show that the inner core of the nucleolus and the NR lose integrity upon CPV infection, whereas the peripheral layers remain relatively intact. This suggests that, in contrast to HSV-1 infection, CPV infection induces only a partial disruption of nucleolar

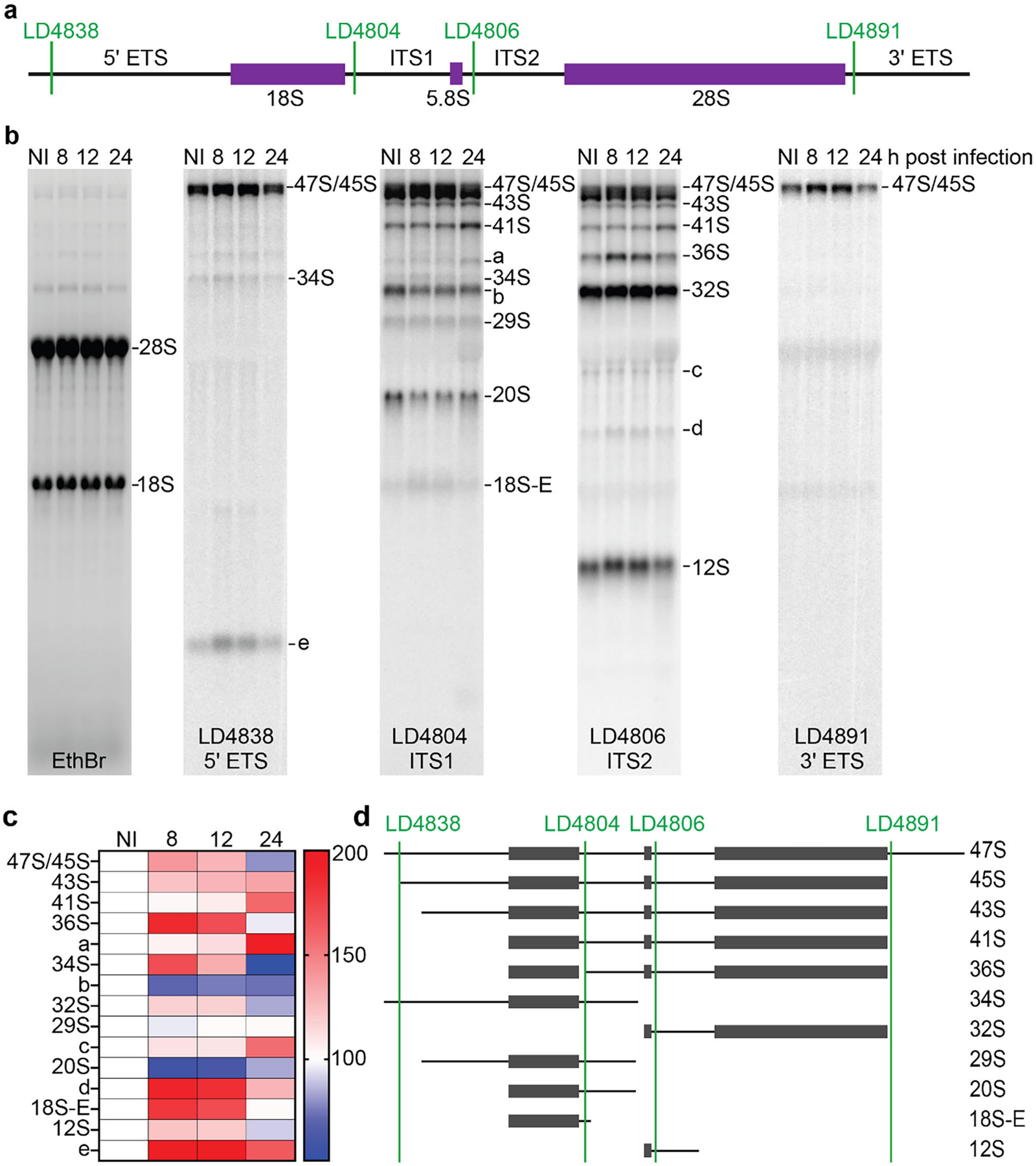

Fig. 7 | Infection alters ribosome biogenesis. a Schematic depiction of the feline 47S pre-rRNA and location of the probes used to detect processing intermediates. The 5′ and 3′ external transcribed spacers (ETS) and internal transcribed spacers (ITS) 1 and 2 are indicated. **b** Total RNA from NLFK cells was extracted at 8, 12, and 24 hpi. A noninfected (NI) sample was used as a control. The RNA was resolved on a denaturing high-resolution agarose gel, stained with ethidium bromide (EthBr) to reveal large mature rRNAs, or processed for northern blotting to detect precursor rRNAs. Probes for each spacer (LD4838, LD4804, LD4806, and LD4891) were designed (see Materials and Methods), revealing primary processing intermediates. Unmapped species are labeled "a" to "e" in order of decreasing size. **c** Phosphorimager quantification of pre-rRNA species detected. The experiment was repeated four times ($n = 4$, see Fig. S7), and the mean values are depicted in the heatmap. A similar processing phenotype can be observed in cells 8 and 12 hpi. At 24 hpi, a different processing phenotype can be observed. **d** Putative pre-rRNA processing pathway in feline cells, based on a closely related vertebrate mouse (Inspired by ref. 118.

integrity. However, the increased circularity of the nucleolar condensates containing NCL, NPM1, and pre-rRNAs indicates a change in phase behavior compatible with altered interfacial dynamics (Fig. 2). These findings suggest that parvovirus infection changes nucleolar organization with consequences on ribosome biogenesis.

The probing of nucleolar ultrastructure by TREx and cryo-SXT revealed that the progression of infection leads to extensive structural remodeling of nucleoli, including condensation of chromatin around the nucleoli. The observation using TREx microscopy showed that the infection also resulted in the emergence of enlarged nucleolar low-protein density interstices and their vacuolar cavities (Figs. 3 and 4). Similar structural changes have been reported in cells subjected to various chemical stressors[98,99]. The emergence of interconnected channels forming a network is compatible with the notion that the nucleolus has been described as a percolated biomolecular condensate. It is interesting to observe that the size and distribution of the internal cavities seem to change drastically, becoming larger upon viral infection as the nucleolus is remodeled. The virus-induced compaction of intranucleolar DNA could limit chromatin accessibility to transcription factors and thereby downregulate the level of rRNA gene transcription. The redistribution of nucleolar UBF1, a regulator of rDNA transcription[47,48], along with chromatin reorganization, may reduce rRNA transcription. However, our findings show that the total intensity of nucleolar rRNA and the production of primary rRNA transcripts remain relatively unchanged in infection. This may suggest that the partial compaction of intranucleolar chromatin in infected cells does not necessarily lead to significant interference with rRNA transcription. However, we reveal that infection impacts the pre-rRNA processing pathway.

During the infection of various viruses, several proteins localize to the nucleolus, where they interact with nucleolar proteins[32,100]. These interactions lead to the virus-induced disruption of nucleolar function and recruitment of cellular proteins to aid viral replication. During henipavirus infection (a member of the RNA virus family *Paramyxoviridae*), the viral matrix proteins interact with Treacle, a nucleolar protein that regulates rDNA transcription[101]. The acquisition of Treacle during evolution was suggested to coincide with the emergence of the FC subcompartment of the nucleolus[20,102]. In HSV-1 infection, NPM1 translocation outside of the nucleolus is assisted by the viral protein UL24, and that of NCL by viral ICP4 and US11[33,35,93]. The Epstein-Barr virus protein EBNA11 recruits NPM1 for transcriptional activation of its latency genes[103].

Detailed analysis of CPV NS2 interactome[67] suggested that NS2 interacts with several proteins of the nucleolar inner core, peripheral layers, and NR (Fig. 5 and Mattola et al.). These putative nucleolar interactors of NS2 are involved in nucleolar organization and pre-rRNA processing. A major NS2 interactor is Ki-67, a protein critical for nucleolar homeostasis during both interphase and mitosis. In interphase, Ki-67 localizes at the chromatin/nucleolus interface, placing it in an ideal position to help shape the nucleolus. Interestingly, Ki-67 depletion results in nucleolar rounding and loss of perinucleolar chromatin. We also observed nucleolar rounding upon CPV infection; however, in this case, there was a thickening of the perinucleolar chromatin (see Fig. 3a). During mitosis, Ki-67 is essential for nucleolar reassembly. Its depletion leads to the loss of the perichromosomal region, an intermediate stage in nucleolar reformation that consists largely of nucleolar proteins coating the condensed chromosomes[58].

NS2 was also associated with cellular proteins involved in ribosome biogenesis and rRNA processing, whose subcellular distribution was modified upon CPV infection (Fig. 6). The interaction of NS2 with proteins involved in nucleolar organization suggests that NS2 has a role in the profound alterations of nucleolar morphology and function.

Alterations to nucleolar structure during CPV infection was correlated with inhibition of nucleolar function (Fig. 7). We observed a transient change in the steady-state levels of several pre-rRNA precursors, consistent with inhibition at multiple specific processing steps. Notably, these effects were most evident at 8 and 12 hpi but were largely absent at later time points. By 24 hpi, the steady-state levels of most pre-rRNAs had returned close to normal, even though nucleolar structure remained profoundly altered. There are two possible explanations for this observation: (1) the kinetics of CPV infection are compatible with the virus having already imposed most of its stress on host nucleolar processes by ~12 h (through viral replication, gene expression, and cytopathic effects). At later stages, host compensatory responses, depletion of viral replication factors, or saturation of viral gene expression may relieve part of the stress, allowing partial restoration of nucleolar activity; and (2) given the lytic nature of CPV, by 24 hpi a fraction of infected cells may already be lost, so that the observed signal predominantly reflects surviving or partially damaged cells. While these explanations are not mutually exclusive, we favor the first scenario because we still observed a strong accumulation of the 41S pre-rRNA at 24 h (Fig. 7).

Why might it be interesting for the virus to repress host cell ribosome biogenesis during infection? Firstly, it is essential to consider that ribosomes are long-lived (i.e., several days) ribonucleoprotein particles that are robustly packaged during assembly. This implies that pre-existing ribosomes remain available to produce the viral components throughout infection. Secondly, ribosome biogenesis is an energy-intensive process that engages most cellular activities, including all three RNA polymerases and hundreds of factors involved in RNA cleavage, modification, folding, and transport—some are also essential for other cellular substrates. Additionally, ribosome biogenesis spans multiple cellular subcompartments: it begins in the nucleolus, continues in the nucleoplasm, and is finalized in the cytoplasm. Thus, it is reasonable to assume that suppressing ribosome biogenesis, at least temporarily, is beneficial for the virus, as it reduces the host cell's energy expenditure and redirects resources toward processes that favor viral replication.

In conclusion, our work demonstrates that autonomous parvoviruses, such as CPV, not only remodel the structural organization of the nucleolus but also modulate its function. This study provides insights into the functional and physical interactions between autonomous parvoviruses and the nucleolus.

Materials and methods

Cell lines, plasmids, and viruses

NLFK cells were maintained in Dulbecco's Modified Eagle Medium supplemented with 10% fetal calf serum, 1% penicillin/streptomycin, and 1% L-glutamine (Gibco, Thermo Fisher Scientific, Waltham, MA, USA). The cells were kept at 37 °C in 5% CO_2 and passaged three times a week. Infectious plasmid clone pBI265[104] was used to generate CPV-2. Cells were transfected using JetOptimus transfection reagent (Polyplus-transfection, Illkirch, France) as described in the manufacturer's instructions. Virus stocks were produced in NLFK cells and concentrated using an Amicon® Stirred Cell ultrafiltration system (Merck KGaA, Darmstadt, Germany).

Antibodies

The following primary antibodies against viral antigens used in confocal microscopy analyses were generous gifts: mouse anti-NS1 (Dr. Caroline Astell, University of British Columbia, Vancouver, Canada)[105]. mouse anti-NS2 and rabbit anti-VP2 (Dr. Colin Parrish, Cornell University, Ithaca, NY, USA)[60,106]. Commercial primary antibodies against cellular proteins were used according to the manufacturer's instructions: rabbit UBF1 (ab244287, Abcam, Cambridge, UK), rabbit FBL (ab166630, Abcam), rabbit NCL (ab22758, Abcam), mouse NPM1 (conjugated to Alexa647, MA3-25200-A647, Invitrogen, Life Technologies, Waltham, MA), rabbit Ki-67 (ab15580, Abcam), mouse rRNA (MA1-16628, Invitrogen)[107], rabbit DDX27 (17087-1-AP, ProteinTech Europe, MA, UK), rabbit EBNA1BP2 (PA5-97189, Invitrogen), rabbit NIFK (HPA 035735, Sigma, Merck KGaA). The primary antibodies were followed by goat anti-mouse or anti-rabbit Alexa448, Alexa546, and Alexa647 conjugated secondary antibodies (Thermo Fisher Scientific, Waltham, MA, USA).

Immunolabelling and confocal microscopy

For microscopy sample preparation, NLFK cells were cultured on glass coverslips at 37 °C with 5% CO_2. Cells were infected with CPV and fixed at 8, 12, or 24 hpi in 4% paraformaldehyde for 12 min. Following fixation, cells were permeabilized with 0.1% Triton X-100 in phosphate-buffered saline supplemented with 0.5% bovine serum albumin (BSA). After primary antibody immunolabeling, cells were labeled with mouse or anti-rabbit secondary fluorescent antibodies. DNA was stained with Pro-Long Diamond anti-fade media with DAPI (Thermo Fisher Scientific).

The microscopy of immunolabeled samples was performed with Leica TCS SP8 FALCON (Leica Microsystems, Mannheim, Germany) and Nikon A1R (Nikon, Tokyo, Japan) laser scanning confocal microscopes. The parameters for images acquired with Leica TCS SP8 FALCON were as follows: DAPI was excited with a 405 nm diode laser, and the fluorescence was collected between 415 and 495 nm. Alexa488 and Alexa546 were excited with 499 and 557 nm wavelengths of pulsed white light laser (80 MHz). The emission detection range was adjusted to 505–561 nm for Alexa488 and 568–648 nm for Alexa546. Microscopy images with Nikon were acquired by exciting DAPI with a 405 nm diode laser and collecting with a 450/50 nm band-pass filter. Alexa488 was excited with a 488 nm argon laser, and the fluorescence was collected with a 515/30 nm band-pass filter. Alexa546 was excited with a 561 nm sapphire laser and detected with a 595/50 nm band-pass filter. Alexa647 was excited with a 640 nm diode laser and detected with a 660 long-pass filter. The image resolution was 512 × 512 or 1024 × 1024 pixels, with a pixel size between 30 and 60 nm in the *x*- and *y*-directions and 180–300 nm in the *z*-direction. A fixed optical configuration was used to acquire all images of the same sample set.

The nuclei were segmented from the DAPI stain using Otsu's or the minimum cross-entropy method[108,109]. Total fluorescence intensities in the nucleus and nucleoli were calculated by summing the pixel intensity values within the segmented regions. The foci of nucleolar proteins were segmented by adjusting the intensity threshold to 33, 45, and 55% of the intensity range in each nucleus for UBF1, fibrillarin, and nucleolin, respectively. rRNA signal was segmented using Otsu's algorithm. The intensity distributions of labels with respect to the nuclear or nucleolar border were determined by calculating the shortest distance of each pixel to the border and calculating the mean intensity as a function of the distance using 2-pixel-wide distance bins for averaging. Due to the flat shape of fixed cells, the confocal section with the largest nuclear area was selected for the analyses of intensity with respect to the nuclear border, and 2D Euclidean distance was used as a metric. Since there can be many nucleoli in one cell and the nucleoli can lie on various confocal planes, the whole 3D stack was used in the analyses for the nucleolar border, and 3D Euclidean distance was used as a metric. Correlations between DNA staining and antibody labels were determined by using Pearson correlation coefficients in the nuclear region. For all the analyses, the given statistics were calculated over cells. The circularity of the single planes of segmented rRNA antibody-labeled nucleoli was determined with Fiji[110]. Circularity determination in Fiji is based on the equation $4\pi(\text{area per perimeter}^2)$, where a perfect circle is indicated by the value 1.0.

Ten-fold robust expansion microscopy and visualization

NLFK cells were grown on coverslips as previously. Noninfected and infected cells were fixed at 24 hpi in 4% PFA (EM Sciences, SKU 15710, diluted to 4% with sterile PBS) for 12 min at room temperature, after which the cells were permeabilized with 0.5% Triton X-100 in PBS supplemented with 0.5% BSA. The permeabilized cells were immunolabelled with mouse anti-NS1 and rabbit anti-fibrillarin primary antibodies, and anti-mouse Alexa546 and anti-rabbit Alexa448 secondary antibodies. Primary and secondary antibodies were used at 3-fold and 4-fold higher concentrations, respectively, compared to standard immunolabeling.

Ten-fold Robust Expansion Microscopy was performed according to the protocol described earlier[68]. Briefly, immunolabeled samples on glass coverslips were anchored using 0.1 mg/ml Acrolyl-X (Invitrogen, Catalog number A20770) overnight at +4 °C. Gelation was performed with a gel containing 14.2% acrylamide (Sigma-Aldrich, product number A9099), 10.1% sodium acrylate (AmBeed, catalog number A107105), 0.005% bis-acrylamide (Sigma-Aldrich, product number M1533), 0.15% ammonium persulfate (Sigma-Aldrich, A3678), and 0.15% TEMED (Sigma-Aldrich, product number T22500) in PBS for 1 h at 37 °C. After gelation, the samples were denatured in 0.2 M NaCl, 50 mM Tris (pH 6.8), and 5.76% SDS for 1.5 h at 78 °C and washed twice with PBS. Gels were stained for the total protein with 20 μg/ml of ATTO 647 N NHS (Atto-tec, Siegen, Germany) dye in sodium bicarbonate buffer (Sigma) for 1 h at RT. DAPI (Roche) diluted 1:6000 in PBS was used to stain DNA for 60 min before the expansion. Gels were expanded in distilled H_2O, changing the water until no further expansion was observed. The achieved expansion factor (approximately 7.5) was calculated by comparing the gel size after the gelation and after the expansion and back-calculated into image scale bars.

Images of expansion samples were acquired with a Leica SP8 confocal microscope using the 63x water immersion objective (1.2 NA). DAPI was excited with a 405 nm laser and detected with a PMT detector at 412–480 nm. Alexa 488 was excited with a 499 nm laser and detected at 506–552 nm using a Leica HyD SMD detector. Alexa 546 was excited with a 557 nm laser and detected at 566–611 nm using a Leica HyD SMD detector. The total protein stain was excited with a 645 nm laser and detected at 652–800 nm using a Leica HyD SMD detector. The pixel size was 90 nm in the *x*- and *y*-directions and 356 nm in the *z*-direction. The images were first denoised using a Gaussian filter with a radius of three pixels to analyze the DNA and total protein labels in the nucleoli. Then, the nucleoli were segmented by setting an intensity threshold for the total protein channel using Otsu's algorithm[108]. In segmenting cells with contiguous nucleoli and a strong total protein signal at the nuclear envelope, the total protein images were manually edited to remove continuity and prevent the segmentation of other regions besides the nucleoli. The coefficient of variation (the standard deviation divided by the mean) for the DNA and total protein labels and the Pearson correlation coefficient were calculated for the pixels belonging to the segmented nucleolar region. The intensity of the labels for the nucleolar border was analyzed by calculating the minimum distance of each pixel to this border, grouping the pixels based on their distance to the border, and calculating the mean intensity of each group. Surface renderings of the noninfected and infected nucleoli were created with Dragonfly 3D World v2024.1.

Cryo-SXT of adherent cells on grids

NLFK cells were grown and infected with CPV for 24 h at 37 °C on Au grids (Quantifoil-coated Au-TEM finder grids, R2/2, G200F1, Gilder, Jena, GER). Noninfected and infected cells were fixed with 4% PFA for 12 min at room temperature and labeled with 1 μg/ml Hoechst 33342. The infected cells were identified by an infection-induced chromatin marginalization using a widefield microscope (Leica DM IL LED, Leica Microsystems GmbH, Germany) with HC FL PLAN 40X/0.65NA air objective or a confocal microscope (Leica SP 8, Leica Microsystems GmbH, Germany) with HC PL APO 63x/1.2NA water immersion objective. The grids were plunged into liquid ethane for vitrification (Leica EM GP2, Leica Microsystems GmbH, Germany) and kept at −196 °C until imaging. Using a compact soft X-ray microscope, the pre-vitrification-located infected cells were re-located by a low magnification SXT imaging, and a built-in cryo-fluorescence microscopy from the vitrified grids, and tomographic tilt-series of infected cells were collected (SXT100, Sirius XT, Dublin, IRE, https://siriusxt.com/)[111,112]. The tilt series was acquired assets of X-ray projections covering a 120° tilt range with 1° increments. The exposure per projection ranged from 15 to 60 s, depending on the sample ice thickness and tilt angle. The exposure time was increased to 120 s at high tilt angles for samples with particularly thick ice. The samples were maintained at temperatures of −163 °C or lower throughout all experimental stages. The tomographic data alignment and data analysis were done as described in detail[113].

BioID analyses

BioID of CPV NS2 protein was performed as previously described[67]. Briefly, a biotin protein ligase was fused to NS2 to allow for the detection of proximal and interacting proteins by biotin tags. The high-confidence NS2 interactions identified among the biotinylated proteins were further screened for nucleolar interactors. Data was analyzed with SAINTexpress[114], and filtered using a protein-level Bayesian FDR of 0.05 as the cutoff. Controls included four different GFP-BirA* constructs, including NLS-GFP. Further filtering was done by integrating control experiment data from the CRAPome contaminant repository[115]. Interactors detected in over 20% of background experiments from CRAPome were discarded, unless their average spectral count in the collected data was more than three times higher than in the background experiments. The high-confidence interactor set was used for Protein ANalysis Through Evolutionary Relationships (PANTHER) classification system (http://www.pantherdb.org/) to create a GO biological process annotation chart of NS2 interactors (Supplementary Data 1).

Proximity ligation assay (PLA)

The association of NS2 with the key interactor Ki-67 during infection was verified with PLA. NLFK cells were grown on coverslips and infected with CPV. Infected and noninfected samples were fixed at 24 hpi in 4% formaldehyde for 12 min and permeabilized using 0.1% Triton X-100 in PBS. NS2 and Ki-67 were identified with mouse anti-NS2 and rabbit anti-Ki-67 antibodies, respectively, and the assay was performed using the Duolink In Situ Orange Mouse/Rabbit kit (Merck KGaA) following the manufacturer's protocol. Technical controls were prepared from infected samples by omitting the anti-NS2 antibody or by omitting the PLA probes. Samples were embedded into a non-hardening mounting medium containing DAPI and imaged with a Nikon A1R confocal microscope with Plan Apo VC 60x oil immersion objective (NA 1.4). The human-in-the-loop machine-learning-based characterization of DAPI-labeled chromatin distribution verified the infection in PLA-labeled cells. The machine learning model was built, trained, and tested using Keras 1.0 with TensorFlow 2.0 backend using Python 3.9 in the Google Colab pro-environment. The deep learning code and model developed in this study can be found at https://github.com/leclercsimon74/Infection_Prediction_CPV. DAPI was excited with a 405 nm diode laser, and the fluorescence was collected with a 450/50 nm band-pass filter. PLA signals were excited with a 561 nm sapphire laser, and the fluorescence was collected with a 595/50 nm band-pass filter. Single cells were imaged as stacks (resolution 512 × 512 pixels, pixel size in xy 60 nm, z sampling distance 200 nm).

DAPI signal was used to segment the nuclei from image stacks by automatic minimum cross entropy segmentation[109] and filling any holes within the segmented regions. The PLA signals were segmented using the maximum entropy algorithm[116], and their geometric centers were determined. The number of PLA signals with their geometric center located within the segmented nucleus was counted.

Western blot

0.6×10^6 NLFK cells per plate were seeded 20 h prior to infection. Infected and noninfected control cells were collected by scraping at 24 hpi, resuspended in Laemmli Sample Buffer (Bio-Rad Laboratories, USA) in PBS, heated at 95 °C for 10 min, and stored at −80 °C. Lysate volumes of 25 µl from three biological replicate experiments were loaded onto 4–20% Mini Protean TGX Stain-Free gels (Bio-Rad Laboratories, USA), and proteins were separated by electrophoresis at 100 V for 80 min. Proteins were transferred onto 0.2 µm polyvinylidene difluoride membranes using the pre-assembled Trans-Blot Turbo Transfer Pack (Bio-Rad Laboratories, USA) and Trans-Blot Turbo Transfer-System (Bio-Rad Laboratories, USA). Gels were re-imaged to verify protein transfer. Membranes were blocked for 10 min in EveryBlot Blocking Buffer (Bio-Rad Laboratories, USA) and probed with primary antibodies against DDX27 (1:500), NIFK (0.4 µg/ml), and CPV NS1 (1:1000), or EBNA1BP2 (1:1000) and CPV NS1 (1:1000). Protein bands were visualized with fluorophore-conjugated secondary antibodies, goat anti-mouse IgG StarBright Blue 520 and goat anti-rabbit IgG StarBright Blue 700 (Bio-Rad Laboratories, USA), used at a dilution of 1:2500 and imaged with the Bio-Rad ChemiDoc MP Imaging System. Band intensities were quantified using Image Lab 6.1 software (Bio-Rad Laboratories, USA) and normalized against the total protein intensity of the corresponding lane obtained from the gel image. Statistical significances were determined with GraphPad Prism software using the Welch's *t*-test.

Quantitative northern blotting analysis of pre-rRNA

Total RNA was extracted from noninfected and infected NLFK cells at 8, 12, and 24 hpi with TRI reagent solution (Thermofisher), according to the manufacturer's instructions. To analyze high-molecular-weight RNAs, 5 µg total RNA was resolved in a 1.2% formaldehyde-agarose denaturing gel, followed by electrophoresis at 65 V. Agarose gels were transferred overnight by capillarity onto Hybond-N+ membranes (Cytiva) in 10x saline sodium citrate. Membranes were prehybridized at 65 °C for 1 h in a solution containing 50% formamide, 5x SSPE, 5x Denhardt's solution, 1% (wt/vol) SDS, and 200 mg/ml fish sperm DNA (Roche). Hybridization with specific ^{32}P-labeled oligonucleotide probes was carried out for 1 h at 65 °C and overnight at 37 °C. The probes LD4838, LD4804, LD4806, and LD4891 were designed using the Felis catus_Fca126_mat1.0 genome (NCBI RefSeq assembly: GCF_018350175.1). Probe sequences are listed in Supplementary Table 1. The membranes were washed and exposed to Fuji imaging plates (Fujifilm). Signals were captured with a Phosphorimager (FLA-7000, Fujifilm) and quantified with Multi Gauge Software (Fujifilm, v 3.1).

Statistics and reproducibility

Sample sizes, exact *p*-values, and statistical testing methods are reported in each corresponding figure legend. For basic immunolabeling studies, image data from two to four independent biological replicate experiments were pooled for analyses. Northern and Western blotting studies were performed using cell lysate samples from three to four independent biological replicate experiments. The more challenging SXT and ExM studies were done with cell samples from a single experiment.

Reporting summary

Further information on research design is available in the Nature Portfolio Reporting Summary linked to this article.

Data availability

Image datasets are available in the BioImage Archive (https://www.ebi.ac.uk/bioimage-archive/) under accession number S-BIAD2342[117]. Unedited images of gels and blots (Supplementary Fig. 9) and the numerical data used for the graphs (Supplementary Data 4) are available.

Code availability

The deep learning code and model developed in this study for verifying CPV-infected cells by a characteristic nuclear DAPI staining pattern is available at https://github.com/leclercsimon74/Infection_Prediction_CPV.

Received: 8 May 2025; Accepted: 5 December 2025;

References

1. Boyne, J. R. & Whitehouse, A. Nucleolar disruption impairs Kaposi's sarcoma-associated herpesvirus ORF57-mediated nuclear export of intronless viral mRNAs. *FEBS Lett.* **583**, 3549–3556 (2009).
2. Pearson, A., Bourget, A., Ben Abdeljelil, N. & Lymberopoulos, M. H. Role of the viral protein UL24 in nucleolar modifications induced by herpes simplex virus 1. *BMC Proc.* **5**, P102 (2011).
3. Lee, T. W. R., Blair, G. E. & Matthews, D. A. Adenovirus core protein VII contains distinct sequences that mediate targeting to the nucleus and nucleolus, and colocalization with human chromosomes. *J. Gen. Virol.* **84**, 3423–3428 (2003).
4. Hindley, C. E., Davidson, A. D. & Matthews, D. A. Relationship between adenovirus DNA replication proteins and nucleolar proteins B23.1 and B23.2. *J. Gen. Virol.* **88**, 3244–3248 (2007).
5. Lawrence, F. J., McStay, B. & Matthews, D. A. Nucleolar protein upstream binding factor is sequestered into adenovirus DNA replication centres during infection without affecting RNA polymerase I location or ablating rRNA synthesis. *J. Cell Sci.* **119**, 2621–2631 (2006).
6. Wistuba, A., Kern, A., Weger, S., Grimm, D. & Kleinschmidt, J. A. Subcellular compartmentalization of adeno-associated virus type 2 assembly. *J. Virol.* **71**, 1341–1352 (1997).
7. Johnson, J. S. & Samulski, R. J. Enhancement of adeno-associated virus infection by mobilizing capsids into and out of the nucleolus. *J. Virol.* **83**, 2632–2644 (2009).

8. Dubois, M.-L. & Boisvert, F.-M. The nucleolus: structure and function. in *The Functional Nucleus* (eds. Bazett-Jones, D. P. & Dellaire, G.) 29–49 (Springer International Publishing, Cham, 2016).
9. Raska, I., Shaw, P. J. & Cmarko, D. Structure and function of the nucleolus in the spotlight. *Curr. Opin. Cell Biol.* **18**, 325–334 (2006).
10. Lafontaine, D. L. J. Birth of nucleolar compartments: phase separation-driven ribosomal RNA sorting and processing. *Mol. Cell* **76**, 694–696 (2019).
11. Yao, R.-W. et al. Nascent Pre-rRNA sorting via phase separation drives the assembly of dense fibrillar components in the human nucleolus. *Mol. Cell* **76**, 767–783.e11 (2019).
12. Qi, Y. & Zhang, B. Chromatin network retards nucleoli coalescence. *Nat. Commun.* **12**, 6824 (2021).
13. Padeken, J. & Heun, P. Nucleolus and nuclear periphery: velcro for heterochromatin. *Curr. Opin. Cell Biol.* **28**, 54–60 (2014).
14. Caragine, C. M., Haley, S. C. & Zidovska, A. Nucleolar dynamics and interactions with nucleoplasm in living cells. *Elife* **8**, e47533 (2019).
15. Peng, T. et al. Mapping nucleolus-associated chromatin interactions using nucleolus Hi-C reveals pattern of heterochromatin interactions. *Nat. Commun.* **14**, 350 (2023).
16. Pederson, T. The nucleolus. *Cold Spring Harb. Perspect. Biol.* **3**, a000638 (2011).
17. Hernandez-Verdun, D. Assembly and disassembly of the nucleolus during the cell cycle. *Nucleus* **2**, 189–194 (2011).
18. Shan, L. et al. Nucleolar URB1 ensures 3’ ETS rRNA removal to prevent exosome surveillance. *Nature* **615**, 526–534 (2023).
19. Lafontaine, D. L. J. In phase with the nucleolus. *Cell Res.* **33**, 579–580 (2023).
20. Lafontaine, D. L. J. When two became three: shaping the nucleolus with Treacle. *Cell Rep.* **42**, 113060 (2023).
21. Stenström, L. et al. Mapping the nucleolar proteome reveals a spatiotemporal organization related to intrinsic protein disorder. *Mol. Syst. Biol.* **16**, e9469 (2020).
22. Feric, M. et al. Coexisting liquid phases underlie nucleolar subcompartments. *Cell* **165**, 1686–1697 (2016).
23. Falahati, H. & Wieschaus, E. Independent active and thermodynamic processes govern the nucleolus assembly in vivo. *Proc. Natl. Acad. Sci. USA* **114**, 1335–1340 (2017).
24. Lafontaine, D. L. J., Riback, J. A., Bascetin, R. & Brangwynne, C. P. The nucleolus as a multiphase liquid condensate. *Nat. Rev. Mol. Cell Biol.* **22**, 165–182 (2021).
25. Strom, A. R. & Brangwynne, C. P. The liquid nucleome—phase transitions in the nucleus at a glance. *J. Cell Sci.* **132**, jcs235093 (2019).
26. Phair, R. D. & Misteli, T. High mobility of proteins in the mammalian cell nucleus. *Nature* **404**, 604–609 (2000).
27. Andersen, J. S. et al. Nucleolar proteome dynamics. *Nature* **433**, 77–83 (2005).
28. Boisvert, F.-M., van Koningsbruggen, S., Navascués, J. & Lamond, A. I. The multifunctional nucleolus. *Nat. Rev. Mol. Cell Biol.* **8**, 574–585 (2007).
29. Iarovaia, O. V. et al. Nucleolus: a central hub for nuclear functions. *Trends Cell Biol.* **29**, 647–659 (2019).
30. Boulon, S., Westman, B. J., Hutten, S., Boisvert, F.-M. & Lamond, A. I. The nucleolus under stress. *Mol. Cell* **40**, 216–227 (2010).
31. Scherl, A. et al. Functional proteomic analysis of human nucleolus. *Mol. Biol. Cell* **13**, 4100–4109 (2002).
32. Salvetti, A. & Greco, A. Viruses and the nucleolus: the fatal attraction. *Biochim. Biophys. Acta* **1842**, 840–847 (2014).
33. Callé, A. et al. Nucleolin is required for an efficient herpes simplex virus type 1 infection. *J. Virol.* **82**, 4762–4773 (2008).
34. Lymberopoulos, M. H. & Pearson, A. Involvement of UL24 in herpes-simplex-virus-1-induced dispersal of nucleolin. *Virology* **363**, 397–409 (2007).
35. Greco, A. et al. Nucleolin interacts with US11 protein of herpes simplex virus 1 and is involved in its trafficking. *J. Virol.* **86**, 1449–1457 (2012).
36. Biggiogera, M. et al. Nucleolar distribution of proteins B23 and nucleolin in mouse preimplantation embryos as visualized by immunoelectron microscopy. *Development* **110**, 1263–1270 (1990).
37. Ginisty, H., Sicard, H., Roger, B. & Bouvet, P. Structure and functions of nucleolin. *J. Cell Sci.* **112**, 761–772 (1999).
38. Srivastava, M. & Pollard, H. B. Molecular dissection of nucleolin’s role in growth and cell proliferation: new insights. *FASEB J.* **13**, 1911–1922 (1999).
39. Jia, W., Yao, Z., Zhao, J., Guan, Q. & Gao, L. New perspectives of physiological and pathological functions of nucleolin (NCL). *Life Sci.* **186**, 1–10 (2017).
40. Daniely, Y. & Borowiec, J. A. Formation of a complex between nucleolin and replication protein A after cell stress prevents initiation of DNA replication. *J. Cell Biol.* **149**, 799–810 (2000).
41. Chen, D. & Huang, S. Nucleolar components involved in ribosome biogenesis cycle between the nucleolus and nucleoplasm in interphase cells. *J. Cell Biol.* **153**, 169–176 (2001).
42. Galibert, M. D., Carreira, S. & Goding, C. R. The Usf-1 transcription factor is a novel target for the stress-responsive p38 kinase and mediates UV-induced Tyrosinase expression. *EMBO J.* **20**, 5022–5031 (2001).
43. Yang, K. et al. A redox mechanism underlying nucleolar stress sensing by nucleophosmin. *Nat. Commun.* **7**, 13599 (2016).
44. Yao, Z. et al. B23 acts as a nucleolar stress sensor and promotes cell survival through its dynamic interaction with hnRNPU and hnRNPA1. *Oncogene* **29**, 1821–1834 (2010).
45. Roussel, P., André, C., Masson, C., Géraud, G. & Hernandez-Verdun, D. Localization of the RNA polymerase I transcription factor hUBF during the cell cycle. *J. Cell Sci.* **104**, 327–337 (1993).
46. Tuan, J. C., Zhai, W. & Comai, L. Recruitment of TATA-binding protein-TAFI complex SL1 to the human ribosomal DNA promoter is mediated by the carboxy-terminal activation domain of upstream binding factor (UBF) and is regulated by UBF phosphorylation. *Mol. Cell Biol.* **19**, 2872–2879 (1999).
47. Sanij, E. & Hannan, R. D. The role of UBF in regulating the structure and dynamics of transcriptionally active rDNA chromatin. *Epigenetics* **4**, 374–382 (2009).
48. Sanij, E. et al. UBF levels determine the number of active ribosomal RNA genes in mammals. *J. Cell Biol.* **183**, 1259–1274 (2008).
49. Lafontaine, D. L. & Tollervey, D. Synthesis and assembly of the box C +D small nucleolar RNPs. *Mol. Cell Biol.* **20**, 2650–2659 (2000).
50. Omer, A. D., Ziesche, S., Ebhardt, H. & Dennis, P. P. In vitro reconstitution and activity of a C/D box methylation guide ribonucleoprotein complex. *Proc. Natl. Acad. Sci. USA* **99**, 5289–5294 (2002).
51. Tollervey, D., Lehtonen, H., Jansen, R., Kern, H. & Hurt, E. C. Temperature-sensitive mutations demonstrate roles for yeast fibrillarin in pre-rRNA processing, pre-rRNA methylation, and ribosome assembly. *Cell* **72**, 443–457 (1993).
52. Lindström, M. S. NPM1/B23: a multifunctional chaperone in ribosome biogenesis and chromatin remodeling. *Biochem. Res. Int.* **2011**, 195209 (2011).
53. Mitrea, D. M. et al. Nucleophosmin integrates within the nucleolus via multi-modal interactions with proteins displaying R-rich linear motifs and rRNA. *Elife* **5**, e13571 (2016).
54. Mitrea, D. M. et al. Self-interaction of NPM1 modulates multiple mechanisms of liquid–liquid phase separation. *Nat. Commun.* **9**, 842 (2018).
55. Verheijen, R. et al. Ki-67 detects a nuclear matrix-associated proliferation-related antigen. II. localization in mitotic cells and association with chromosomes. *J. Cell Sci.* **92**, 531–540 (1989).

56. Kill, I. R. Localisation of the Ki-67 antigen within the nucleolus. Evidence for a fibrillarin-deficient region of the dense fibrillar component. *J. Cell Sci.* **109**, 1253–1263 (1996).
57. Sun, X. & Kaufman, P. D. Ki-67: more than a proliferation marker. *Chromosoma* **127**, 175–186 (2018).
58. Sobecki, M. et al. The cell proliferation antigen Ki-67 organises heterochromatin. *Elife* **5**, e13722 (2016).
59. Cotmore, S. F., Sturzenbecker, L. J. & Tattersall, P. The autonomous parvovirus MVM encodes two nonstructural proteins in addition to its capsid polypeptides. *Virology* **129**, 333–343 (1983).
60. Weichert, W. S. et al. Assaying for structural variation in the parvovirus capsid and its role in infection. *Virology* **250**, 106–117 (1998).
61. Niskanen, E. A., Ihalainen, T. O., Kalliolinna, O., Häkkinen, M. M. & Vihinen-Ranta, M. Effect of ATP binding and hydrolysis on dynamics of canine parvovirus NS1. *J. Virol.* **84**, 5391–5403 (2010).
62. Niskanen, E. A., Kalliolinna, O., Ihalainen, T. O., Häkkinen, M. & Vihinen-Ranta, M. Mutations in DNA binding and transactivation domains affect the dynamics of parvovirus NS1 protein. *J. Virol.* **87**, 11762–11774 (2013).
63. Ihalainen, T. O. et al. Parvovirus induced alterations in nuclear architecture and dynamics. *PLoS ONE* **4**, e5948 (2009).
64. Cotmore, S. F., D'Abramo, A. M., Carbonell, L. F., Bratton, J. & Tattersall, P. The NS2 polypeptide of parvovirus MVM is required for capsid assembly in murine cells. *Virology* **231**, 267–280 (1997).
65. Naeger, L. K., Cater, J. & Pintel, D. J. The small nonstructural protein (NS2) of the parvovirus minute virus of mice is required for efficient DNA replication and infectious virus production in a cell-type-specific manner. *J. Virol.* **64**, 6166–6175 (1990).
66. Eichwald, V., Daeffler, L., Klein, M., Rommelaere, J. & Salomé, N. The NS2 proteins of parvovirus minute virus of mice are required for efficient nuclear egress of progeny virions in mouse cells. *J. Virol.* **76**, 10307–10319 (2002).
67. Mattola, S. et al. Parvovirus nonstructural protein 2 interacts with chromatin-regulating cellular proteins. *PLoS Pathog.* **18**, e1010353 (2022).
68. Damstra, H. G. J. et al. Visualizing cellular and tissue ultrastructure using Ten-fold robust expansion microscopy (TREx). *Elife* **11**, e73775 (2022).
69. Sheard, T. M. D. et al. Differential labelling of human sub-cellular compartments with fluorescent dye esters and expansion microscopy. *Nanoscale* **15**, 18489–18499 (2023).
70. Thiry, M. Ultrastructural distribution of DNA and RNA within the nucleolus of human Sertoli cells as seen by molecular immunocytochemistry. *J. Cell Sci.* **105**, 33–39 (1993).
71. Thiry, M. & Lafontaine, D. L. J. Birth of a nucleolus: the evolution of nucleolar compartments. *Trends Cell Biol.* **15**, 194–199 (2005).
72. Loconte, V. et al. Soft X-ray tomography to map and quantify organelle interactions at the mesoscale. *Structure* **30**, 510–521.e3 (2022).
73. Harkiolaki, M. et al. Cryo-soft X-ray tomography: using soft X-rays to explore the ultrastructure of whole cells. *Emerg. Top. Life Sci.* **2**, 81–92 (2018).
74. Liu, X. et al. An AP-MS- and BioID-compatible MAC-tag enables comprehensive mapping of protein interactions and subcellular localizations. *Nat. Commun.* **9**, 1188 (2018).
75. Söderberg, O. et al. Direct observation of individual endogenous protein complexes in situ by proximity ligation. *Nat. Methods* **3**, 995–1000 (2006).
76. Kellner, M. et al. DEAD-box helicase DDX27 regulates 3' end formation of ribosomal 47S RNA and stably associates with the PeBoW-complex. *Exp. Cell Res.* **334**, 146–159 (2015).
77. Bennett, A. H. et al. RNA helicase, DDX27 regulates skeletal muscle growth and regeneration by modulation of translational processes. *PLoS Genet.* **14**, e1007226 (2018).
78. Uchihara, Y., Tago, K., Tamura, H. & Funakoshi-Tago, M. EBP2, a novel NPM-ALK-interacting protein in the nucleolus, contributes to the proliferation of ALCL cells by regulating tumor suppressor p53. *Mol. Oncol.* **15**, 167–194 (2021).
79. Huber, M. D., Dworet, J. H., Shire, K., Frappier, L. & McAlear, M. A. The budding yeast homolog of the human EBNA1-binding protein 2 (Ebp2p) is an essential nucleolar protein required for pre-rRNA processing. *J. Biol. Chem.* **275**, 28764–28773 (2000).
80. Kim, K.-D. et al. Epigenetic specifications of host chromosome docking sites for latent Epstein-Barr virus. *Nat. Commun.* **11**, 877 (2020).
81. Takagi, M., Sueishi, M., Saiwaki, T., Kametaka, A. & Yoneda, Y. A novel nucleolar protein, NIFK, interacts with the forkhead associated domain of Ki-67 antigen in mitosis. *J. Biol. Chem.* **276**, 25386–25391 (2001).
82. Pan, W.-A. et al. The RNA recognition motif of NIFK is required for rRNA maturation during cell cycle progression. *RNA Biol.* **12**, 255–267 (2015).
83. Mullineux, S.-T. & Lafontaine, D. L. J. Mapping the cleavage sites on mammalian pre-rRNAs: where do we stand?. *Biochimie* **94**, 1521–1532 (2012).
84. Thoms, M. et al. Structural basis for translational shutdown and immune evasion by the Nsp1 protein of SARS-CoV-2. *Science* **369**, 1249–1255 (2020).
85. Matthews, D., Emmott, E. & Hiscox, J. Viruses and the Nucleolus. 321–345 https://doi.org/10.1007/978-1-4614-0514-6_14.(2011)
86. Greco, A. Involvement of the nucleolus in replication of human viruses. *Rev. Med. Virol.* **19**, 201–214 (2009).
87. Hiscox, J. A. RNA viruses: hijacking the dynamic nucleolus. *Nat. Rev. Microbiol.* **5**, 119–127 (2007).
88. Atari, N. et al. Lytic reactivation of the Kaposi's sarcoma-associated herpesvirus (KSHV) is accompanied by major nucleolar alterations. *Viruses* **14**, 1720 (2022).
89. Stow, N. D., Evans, V. C. & Matthews, D. A. Upstream-binding factor is sequestered into herpes simplex virus type 1 replication compartments. *J. Gen. Virol.* **90**, 69–73 (2009).
90. Deffrasnes, C. et al. Genome-wide siRNA screening at biosafety level 4 reveals a crucial role for fibrillarin in henipavirus infection. *PLoS Pathog.* **12**, e1005478 (2016).
91. Lymberopoulos, M. H. & Pearson, A. Relocalization of upstream binding factor to viral replication compartments is UL24 independent and follows the onset of herpes simplex virus 1 DNA synthesis. *J. Virol.* **84**, 4810–4815 (2010).
92. Bender, B. J., Coen, D. M. & Strang, B. L. Dynamic and nucleolin-dependent localization of human cytomegalovirus UL84 to the periphery of viral replication compartments and nucleoli. *J. Virol.* **88**, 11738–11747 (2014).
93. Lymberopoulos, M. H., Bourget, A., Ben Abdeljelil, N. & Pearson, A. Involvement of the UL24 protein in herpes simplex virus 1-induced dispersal of B23 and in nuclear egress. *Virology* **412**, 341–348 (2011).
94. Sagou, K., Uema, M. & Kawaguchi, Y. Nucleolin is required for efficient nuclear egress of herpes simplex virus type 1 nucleocapsids. *J. Virol.* **84**, 2110–2121 (2010).
95. Mattola, S. et al. G2/M checkpoint regulation and apoptosis facilitate the nuclear egress of parvoviral capsids. *Front. Cell Dev. Biol.* **10**, 1070599 (2022).
96. Barrijal, S. et al. Nucleolin forms a specific complex with a fragment of the viral (minus) strand of minute virus of mice DNA. *Nucleic Acids Res.* **20**, 5053–5060 (1992).
97. Qiu, J. & Brown, K. E. A 110-kDa nuclear shuttle protein, nucleolin, specifically binds to adeno-associated virus type 2 (AAV-2) capsid. *Virology* **257**, 373–382 (1999).
98. Jamison, J. M. et al. Nucleolar changes and fibrillarin redistribution following apatone treatment of human bladder carcinoma cells. *J. Histochem. Cytochem.* **58**, 635–651 (2010).

99. Tchelidze, P. et al. Nucleolar sub-compartments in motion during rRNA synthesis inhibition: contraction of nucleolar condensed chromatin and gathering of fibrillar centers are concomitant. *PLoS ONE* **12**, e0187977 (2017).
100. Iarovaia, O. V., Ioudinkova, E. S., Velichko, A. K. & Razin, S. V. Manipulation of cellular processes via nucleolus hijaking in the course of viral infection in mammals. *Cells* **10**, 1597 (2021).
101. Rawlinson, S. M. et al. Viral regulation of host cell biology by hijacking of the nucleolar DNA-damage response. *Nat. Commun.* **9**, 3057 (2018).
102. Jaberi-Lashkari, N., Lee, B., Aryan, F. & Calo, E. An evolutionarily nascent architecture underlying the formation and emergence of biomolecular condensates. *Cell Rep.* **42**, 112955 (2023).
103. Malik-Soni, N. & Frappier, L. Nucleophosmin contributes to the transcriptional activation function of the Epstein-Barr virus EBNA1 protein. *J. Virol.* **88**, 2323–2326 (2014).
104. Parrish, C. R. Mapping specific functions in the capsid structure of canine parvovirus and feline panleukopenia virus using infectious plasmid clones. *Virology* **183**, 195–205 (1991).
105. Yeung, D. E. et al. Monoclonal antibodies to the major nonstructural nuclear protein of minute virus of mice. *Virology* **181**, 35–45 (1991).
106. Wang, D., Yuan, W., Davis, I. & Parrish, C. R. Nonstructural protein-2 and the replication of canine parvovirus. *Virology* **240**, 273–281 (1998).
107. Garden, G. A., Hartlage-Rübsamen, M., Rubel, E. W. & Bothwell, M. A. Protein masking of a ribosomal RNA epitope is an early event in afferent deprivation-induced neuronal death. *Mol. Cell Neurosci.* **6**, 293–310 (1995).
108. Otsu, N. A threshold selection method from gray-level histograms. *IEEE Trans. Syst. Man Cybern.* **9**, 62–66 (1979).
109. Li, C. H. & Lee, C. K. Minimum cross entropy thresholding. *Pattern Recognit.* **26**, 617–625 (1993).
110. Schindelin, J. et al. Fiji: an open-source platform for biological-image analysis. *Nat. Methods* **9**, 676–682 (2012).
111. O'Connor, S. et al. Demonstrating soft X-ray tomography in the lab for correlative cryogenic biological imaging using X-rays and light microscopy. *Sci. Rep.* https://doi.org/10.1038/s41598-025-29385-5 (2025).
112. Fahy, K. et al. Compact cell imaging device (CoCID) provides insights into the cellular origins of viral infections. *J. Phys. Photonics* **3**, 031002 (2021).
113. Leclerc, S. et al. Progression of herpesvirus infection remodels mitochondrial organization and metabolism. *PLoS Pathog.* **20**, e1011829 (2024).
114. Teo, G. et al. SAINTexpress: improvements and additional features in significance analysis of INTeractome software. *J. Proteom.* **100**, 37–43 (2014).
115. Mellacheruvu, D. et al. The CRAPome: a contaminant repository for affinity purification-mass spectrometry data. *Nat. Methods* **10**, 730–736 (2013).
116. Kapur, J. N., Sahoo, P. K. & Wong, A. K. C. A new method for gray-level picture thresholding using the entropy of the histogram. *Computer Vis. Graph. Image Process.* **29**, 273–285 (1985).
117. Huttunen M. et al. Parvovirus infection affects host cell nucleolar organization and ribosome biogenesis. S-BIAD2342, https://doi.org/10.6019/SBIAD2342 (2025).
118. Anikin, L. & Pestov, D. G. 9-Aminoacridine inhibits ribosome biogenesis by targeting both transcription and processing of ribosomal RNA. *Int J. Mol. Sci.* **23**, 1260 (2022).

Acknowledgements

We thank the staff of the Biocenter Finland and Proteomics unit (Helsinki Institute of Life Science, HiLIFE; Institute of Biotechnology Proteomics Unit; Helsinki; Finland) for providing the Bio-ID analysis. This work was financed by the Jane and Aatos Erkko Foundation (M.V.R.), Research Council of Finland under award numbers 330896 (M.V.R.) and 357490 (L.L.), European Union's Horizon 2020 research and innovation programme, Compact Cell Imaging Device (CoCID) under grant agreement No. 101017116 (M.V.R.), the Biocenter Finland, viral gene transfer (M.V.R.), and the Graduate School of the University of Jyvaskyla (S.M.). The funders had no role in the study design, data collection and analysis, the decision to publish, or the preparation of the manuscript. Research in the Lab of D.L.J.L. was supported by the Belgian Fonds de la Recherche Scientifique (F.R.S./FNRS), EOS [CD-INFLADIS, grant n°40007512], Région Wallonne (SPW EER) Win4SpinOff [RIBOGENESIS], the COST actions EPITRAN (CA16120) and TRANSLACORE (CA21154), the European Joint Programme on Rare Diseases (EJP-RD) RiboEurope and DBAGeneCure.

Author contributions

Conceptualization: V.A., S.M., D.L.J.L., and M.V.R. Data curation: S.M., M.H., S.H., A.S., S.K., V.R., and V.A. Formal analysis: S.L., K.S., and V.A. Funding acquisition: C.R.P., D.L.J.F., and M.V.R. Investigation: S.M., M.H., S.H., A.S., A.Z., S.K., V.R., and K.S. Methodology: S.M., S.L., K.S., M.V., K.F., and D.L.J.F. SXT data acquisition: A.Z. Software: S.L., V.A. Resources: M.V., C.R.P., K.F., D.L.J.L., and M.V.R. Project Administration: M.V.R. Visualization: S.M., M.H., and S.H. Writing—original draft preparation: D.L.J.F. and M.V.R. Writing—review and editing: M.H., S.H., L.L., V.A., S.M., D.L.J.L., and M.V.R.

Competing interests

The authors declare no competing interests.

Additional information

Supplementary information The online version contains supplementary material available at https://doi.org/10.1038/s42003-025-09385-x.

Correspondence and requests for materials should be addressed to Denis L. J. Lafontaine or Maija Vihinen-Ranta.

Peer review information *Communications Biology* thanks Ana Pérez-Berná and the other, anonymous, reviewer(s) for their contribution to the peer review of this work. Primary Handling Editors: Juan Fontana and Tobias Goris. A peer review file is available.